J Sol-Gel Sci Technol (2016) 79:328–358
DOI 10.1007/s10971-015-3935-6

ORIGINAL PAPER: CHARACTERIZATION OF GELS, AEROGELS, SOL-GEL DERIVED GLASSES, CERAMICS, HYBRIDS AND COMPOSITES

Synthesis and application of several sol–gel-derived materials via sol–gel process combining with other technologies: a review

Xingzhong Guo[1] · Qilong Zhang[1] · Xingeng Ding[1] · Qianhong Shen[1] · Chunchun Wu[1] · Lingjie Zhang[1] · Hui Yang[1]

Received: 22 July 2015 / Accepted: 9 December 2015 / Published online: 6 January 2016

Abstract Sol–gel process is a very unique wet chemical method for producing advanced materials in various areas of research. An increasingly evolution trend of this process is to combine with other technologies, such as surface modification, hybridization, templating induction, self-assembly, and phase separation, for preparing new materials possessing controllable shape, unique microstructure, superior properties, and special application. The review aims to present the synthesis of several typical sol–gel-derived materials (monodisperse nanoparticles, hybrid coatings, hollow microspheres, aerogels, and porous monoliths) via sol–gel process combining with other technologies. Some examples of application of the sol–gel-derived materials are also included.

Keywords Sol–gel · Surface modification · Hybridization · Templating induction · Self-assembly · Phase separation · Nanoparticle · Hybrid coating · Hollow microsphere · Aerogel · Porous monolith

1 Introduction

Sol–gel process is a very unique wet chemical method for producing advanced materials in various areas of research. This simple, high-purity, low-cost, and low-temperature process dexterously combines the fine control of composition and microstructure at the molecular level with the ability to shape material in bulk, powder, fiber, thin film, and monolith forms. The processed materials can be inorganic, organic, and hybrid, ranging from highly advanced materials to common materials, from optics, electronics, catalysis, separation, energy, space, medicine, sensors, biologics to architecture. This process is attracting more and more attention due to its outstanding advantages and wide application, and its tentacles are extending to the new fields that have not been involved. Sol–gel process is developing to be a multidisciplinary science and technology system owing to its exuberant vitality, and will become one of the most important and promising preparation methods for advanced materials [1–6].

As is well known, sol–gel process commonly involves hydrolysis of precursors (such as metal alkoxides, inorganic salts, and organic polymers), polycondensation to form colloidal sol, sol–gel transition to freeze gel network, drying of wet gel, or/and heat treatment to form crystalline phases. In addition, it is also possible to carry out the purification and stabilization of sol and the strengthening of gel. Some external field conditions such as strong field induction, ultrasonic assistant, microwave assistant, and magnetic field assistant are often used, in some special research areas. In the past decades, a continuing interest for this process is to synthesize all kinds of new materials possessing controllable shape, unique microstructure, superior properties, and special application, through combining with other technologies, such as surface modification, hybridization, templating induction, self-assembly, and phase separation [7–15].

In this review, we demonstrate the synthesis of several typical sol–gel-derived materials (monodisperse nanoparticles, hybrid coatings, hollow microspheres, aerogels, and porous monoliths) via sol–gel process combining with

---

✉ Xingzhong Guo
gxzh_zju@163.com

✉ Hui Yang
yanghui@zju.edu.cn

[1] School of Materials Science and Engineering, Zhejiang University, Hangzhou, People's Republic of China

other technologies. For example, we propose a sol–gel route combining with surface modification to precisely synthesize monodisperse nanoparticles and nanopowders for improving the sintering characterization, microstructure, and mechanical and dielectric properties of electroceramic [16–20], electrical contact materials [21–23], and structural ceramics [24–26] due to unusual nanosize effect. We develop an organic–inorganic hybridization method based on sol–gel technology to prepare many kinds of functional coatings such as antireflection coating [27], anticorrosion coating [28], wearable coating [29–31], and antibacterial coating [32]. We develop a sol–gel self-assembly technology to prepare novel mesoporous silica hollow microspheres inside-loaded Ag nanoparticles that possess good Ag release property and long-term antibacterial activity for antibacterial materials [33]. We adopt a facile one-step route, which is an oil–water (O/W) emulsion process accompanied by sol–gel reaction in the presence of phase separation inducer, to fabricate metallic oxides (TiO_2, ZrO_2, and Al_2O_3) or polymer (ethyl cellulose) hollow microspheres for delivery, adsorption, catalysis, and insulation [35–39]. We present an improved sol–gel route followed by surface modification and atmospheric pressure drying to prepare metallic oxide aerogels (SiO_2/TiO_2, TiO_2, and ZrO_2) [40–42]. We explore the template-free sol–gel process accompanied by phase separation to fabricate hierarchically porous monoliths (SiO_2, TiO_2, and ZrO_2) that have three-dimensional cocontinuous macropores, fine mesoporous structure, and controlled solid skeletons due mainly to their applicability to efficient separation media, flow-through reactors, and anode materials [43–47].

2 The synthesis and application of monodisperse nanoparticles or granules by sol–gel route combining with surface modification or spray-drying

2.1 Introduction

Nanostructure materials exhibit unusual physical and chemical properties, significantly different from those of conventional bulk materials, due to their extremely small size or large specific surface area [48]. Nanosized powders or particles with uniform compositions, no aggregation, and good flowability is one of the key factors for nanostructure materials. So the preparation and characterization of nanoparticles or nanopowders have attracted great attentions, not only for fundamental scientific interest, but also for technological application. Among the preparation methods, sol–gel method displays obvious advantages of obtaining well-defined size and morphology, achieving superior purity, and requiring lower heat treatment temperatures since raw ingredients are microscopically homogeneous from the outset [49–51].

Recent developments in the synthesis of monodispersed, narrow-size-distributed nanoparticles by sol–gel process provide significant boost to development of nanostructure materials by combining with surface modification, in situ doping or spray-drying. These improved processes are widely used to produce pure nanopowders or nanoparticles due to its ability to control the particle size, size distribution, morphology, uniformity, and agglomeration through systematic monitoring of reaction parameters and ingeniously using of dispersion mechanism.

In this work, we propose a sol–gel route combining with surface modification, in situ doping, or spray-drying to precisely synthesize monodisperse nanoparticles, nanopowders, or granules for improving the sintering characterization, microstructure, mechanical and dielectric properties of electroceramic, electrical contact materials, and structural ceramics due to unusual nanosize effect [16–26].

2.2 Preparation and application of monodisperse nanopowders for electroceramics

High-performance electroceramics are necessary for the miniaturization of microwave components. Various electroceramics such as high-permittivity (Ca_{1-x}, $Nd_{2x/3}$)TiO_3 [52, 53], perovskite-structured $BaTiO_3$ [54, 55], and rock salt-structured Li_2TiO_3 [56, 57] have been successively reported. In the previous study, most of the electronic ceramic powders were usually made by standard solid-state reactions or co-precipitation method which requires relatively higher calcination temperature, the powder obtained usually displays large grain size and inferior sinterability. Thus, it was very difficult to obtain a pure electroceramic with high densification, and the porous microstructure caused by evaporation of element and phase transition under high sintering temperature can be detrimental for the further improvement of quality factor. In contrast, sol–gel method starts with a homogeneous liquid solution of cation ingredients, with metal cations mixed in stoichiometric ratios at the atomic scale. Therefore, pure samples at the nanometer scale could theoretically be obtained at lower temperature and shorter reaction time than that afforded by solid-state reaction.

In the present work, we have successfully prepared some typical electronic ceramic nanopowders [(Ca_{1-x}, $Nd_{2x/3}$)TiO_3, ($Nd_{2/3-x}$, Li_{3x})TiO_3, Li_2TiO_3, $BaTiO_3$] by a sol–gel method combining with surface modification [16–20]. In these systems, the polyethylene glycol 400 (PEG 400) was used as a surfactant to inhabit nanoparticles interacting to agglomerate and grow bigger. The resultant nanopowders possess an average particle size below 100 nm, narrow particle size distribution, and high dispersion. The corresponding electronic ceramics prepared by nanopowders can be sintered at a lower temperature, and shows good temperature stability and high electrical properties. Here, we only report an example about the preparation of monodisperse Li_2TiO_3 nanoparticles with an average particle size below 20 nm via a simple sol–gel method in the presence of PEG 400. The phase formation, microstructure, sintering characteristic, and microwave dielectric of Li_2TiO_3 ceramics are investigated systematically [16].

2.2.1 Preparation of monodisperse Li_2TiO_3 nanopowders

In the synthesis procedure, the stoichiometric Li_2TiO_3 compositions were synthesized by a sol–gel method combining with surface modification. PEG 400 as a surfactant was added into the system with 3 wt% of the total solution. The mixed solution was held in water bath at 50 °C until it turned completely to a gel. The gel was dried at 120 °C for 12 h and then was treated at 500–700 °C for 2 h to obtain monodisperse Li_2TiO_3 nanopowders. The resultant Li_2TiO_3 powder from gel heat-treated for 2 h at 500–700 °C exhibits well-defined characteristic peaks assigned to the pure β-Li_2TiO_3 phase (JCPDS card: 33-0831) (Fig. 1), indicating high crystallinity of these samples. With the increase in the heat treatment temperature, the intensity of superstructure lines increases, but no traces of additional phase are visible.

The as-prepared Li_2TiO_3 nanoparticles with PEG 400 (Fig. 2a) were well dispersed, with an average crystal size of 6–12 nm. No obvious aggregation can be observed, and nearly spherical nanoparticles were obtained. However, some of the particles were agglomerated and appeared to be spherical with size 20–50 nm for the sample without PEG 400 (Fig. 2b). This inserted SAED pattern indicates that the spherical nanoparticles are polycrystalline.

Most of the dispersants have a long chain, and when the dispersant is added to the solution during the formation of sol, dispersant can keep the sol particles separated in the solution by adhering to the surface of the particles or absorbing inorganic ions into their network to form nanoparticles. It is established that the formation of metal oxide nanoparticles undergoes two main steps: (1) hydrolysis of metal precursors to produce unstable hydroxyalkoxide, and (2) subsequent condensation reactions by means of olation or oxolation to form M–O–M network. When the PEG 400 is added to the sol, one side of the molecular chain can stick on the surface of the particles while another side keeps dissolved in the solution. Afterward, the particles are wrapped and separated by the shell formed from PEG 400 dispersants. Since the PEG 400 is one kind of glycol which has lots of hydroxyl on its both sides, the existence of a great amount of hydroxyl can lead to the stereo-hindrance effect. Besides, because PEG 400 is nonionic surfactant, the shielding effect which decreases the electrostatic attraction among sol particles also plays an important role during the sol–gel process. These effects can influence the nucleation and growth through the interfacial free energy due to Gibbs–Thomson effects. The surface tension is expected to reduce significantly. As a result, the condensation reactions are reduced correspondingly. Thus, well-distributed particle size can be obtained by controlling the surface free energy during the growth process through the function of dispersant PEG 400.

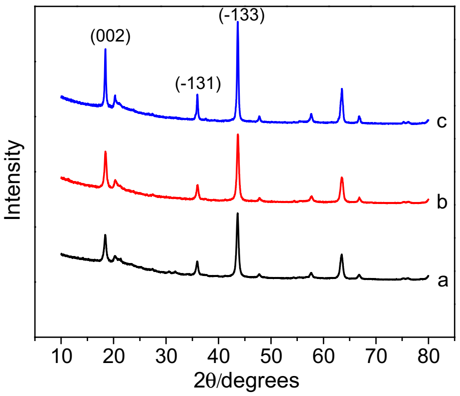

Fig. 1 X-ray diffraction patterns of the stoichiometric Li_2TiO_3 from dried gel heat-treated at *a* 500 °C, *b* 600 °C, and *c* 700 °C for 2 h [16]

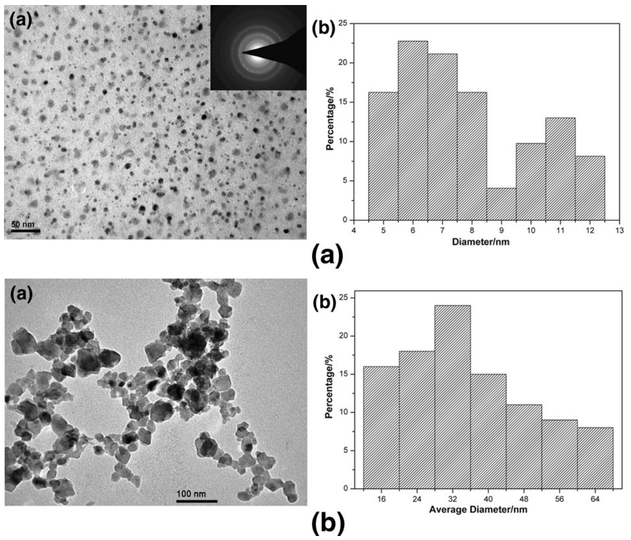

Fig. 2 TEM micrograph and size distribution of Li_2TiO_3 nanoparticles with and without PEG 400 heat-treated at 600 °C for 2 h [16]. **a** With PEG 400. **b** Without PEG 400

2.2.2 *Application of Li_2TiO_3 nanoparticles in microwave electroceramics*

The resulting Li_2TiO_3 nanoparticles were easily densified to produce the Li_2TiO_3 ceramic specimens by pressureless sintering at 1250 °C. There have been previous reports showing that it is very difficult to obtain a pure dense Li_2TiO_3 ceramic under 1300 °C, since much porous microstructures and microcracks will be caused by lithium evaporation and order–disorder phase transition above 1150 °C, with solid-state reacted powder as raw materials. In contrast to that, after sintered at 1250 °C, the Li_2TiO_3 nanopowders synthesized by the sol–gel method could be densified with less micropores and cracks (Fig. 3). This result indicates that the nanoparticles with high ratio specific surface area and surface energy can facilitate the sintering properties and decrease the sintering temperature.

The produced Li_2TiO_3 ceramics shows high microwave dielectric properties (Table 1). In the case of pure Li_2TiO_3 samples, the dielectric constant and quality factor increase with increasing temperature up to 1250 °C. The increase in ε_r and $Q \times f$ is in agreement with the increase in bulk density as shown in the table. As is reported, the optimal dielectric properties of $\varepsilon_r = 23.29$ and $Q \times f = 15{,}525$ GHz were acquired by the conventional solid-state reaction. In addition to that, we have also synthesized the Li_2TiO_3 ceramics by solid-state reaction, and the dielectric properties were $\varepsilon_r = 22.2$, $Q \times f = 18{,}273$ GHz. Compared with the same samples fabricated from a conventional solid-state reaction, the value of quality factor of the stoichiometric sample from nanopowders prepared via the sol–gel method in the investigation is enhanced due to less porosity and high densification.

As shown in our report, the present results confirm that sol–gel process is an effective route to prepare high-quality nanopowders for microwave electroceramics with excellent dielectric properties.

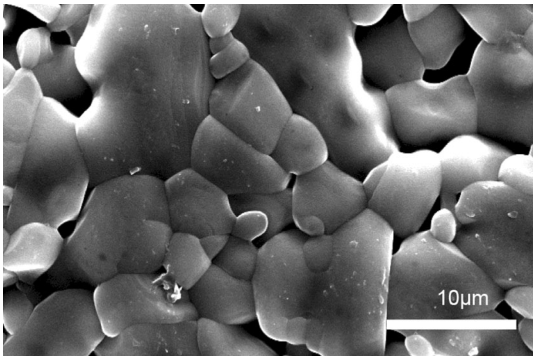

Fig. 3 Scanning electron micrographs of Li_2TiO_3 ceramics sintered at 1250 °C [16]

Table 1 ε_r, $Q \times f$ and ρ of the stoichiometric Li_2TiO_3 ceramics versus T_S [16]

T_S (°C)	ε_r	$Q \times f$ (GHz)	ρ (g/cm^3)
1100	18.7	12,600	3.060
1150	20.6	16,600	3.092
1200	21.9	21,700	3.179
1250	22.2	23,500	3.183

2.3 In situ doping of functional additive by sol coating for microwave ceramics

Doping is an important method in improvement of dielectric properties and sintering characteristics. Generally, the doping additive was introduced by mechanical solid mixing; however, it is very difficult for solid mixture to homogenously disperse a small amount of functional aids in the matrix. In order to improve their electrical properties and homogeneity of electrical ceramics, we developed several kinds of microwave ceramics such as $ZnO–TiO_2$, Al_2O_3, and $CaO–SiO_2$ by preparing the matrix materials using conventional solid-state reaction and adding to a few additives by sol–gel method [19, 20]. Here, the preparation, structure, and dielectric properties of low-temperature-sintered $ZnO–TiO_2$ ceramics doped with $ZnO–B_2O_3–SiO_2$ by sol–gel were described as an example [19].

2.3.1 *Preparation and characteristic of in situ doped powders*

Reagent-grade ZnO and TiO_2 powders were mixed according to the mol ratio of $ZnO:TiO_2 = 1:1.2$ and then calcined at 850 °C for 2 h. The $ZnO–B_2O_3–SiO_2$ sol was prepared as follows: ZnAc, TEOS, and H_3BO_3 were dissolved in ethanol, respectively. Those solutions were mixed with molar ratio of $ZnO:B_2O_3:SiO_2 = 1:2:7$, stirred, and then transparent sol was formed. The calcined $ZnO–TiO_2$ powder was added to the sol, followed by stirring for 60 min and standing for 24 h to transform into colloidal matter. Colloidal matter was dried and calcined at 650 °C for 2 h. As shown in SEM photographs (Fig. 4a) of original calcined powder of $ZnO–TiO_2$, the average particle size of original powder is about 0.8 μm, and the particle shape is irregular. However, it can be observed in Fig. 4b that $ZnO–B_2O_3–SiO_2$ sol was uniformly coated on the surface of $ZnO–TiO_2$ powder, and then, the spherical grains were formed. It indicates that $ZnO–B_2O_3–SiO_2$ additive can be in situ introduced in the $ZnO–TiO_2$ powders by sol coating.

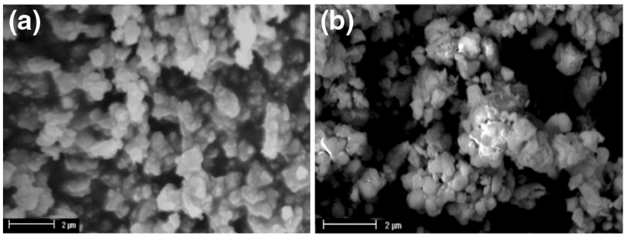

Fig. 4 SEM photographs of **a** original calcined ZnO–TiO_2 powder and **b** calcined ZnO–TiO_2 powder with ZnO–B_2O_3–SiO_2 sol [19]

2.3.2 Sintering characteristic and dielectric properties of in situ doped powders

The synthesized powders were pressed into pellets, and the pellets were subsequently sintered at 900 °C for 3 h in air. As sintering additives, ZnO–B_2O_3–SiO_2 sol and ZnO–B_2O_3–SiO_2 glass are chosen to lower the sintering temperature of ZnO–TiO_2 ceramics effectively from 1100 to 900 °C due to the liquid-phase effect, respectively. For the samples with ZnO–B_2O_3–SiO_2 sol (Fig. 5a), the ZnO–TiO_2 ceramics possesses dense structure with few pores. However, the porous structure occurs in the sample with ZnO–B_2O_3–SiO_2 glass (Fig. 5b). The result indicates that ZnO–B_2O_3–SiO_2 sol can be distributed uniformly in the ZnO–TiO_2 matrix and was sufficient to improve the densification and microstructure of ZnO–TiO_2 ceramic.

Dielectric properties of ZnO–TiO_2 ceramics with ZnO–B_2O_3–SiO_2 sol and ZnO–B_2O_3–SiO_2 glass were, respectively, tested. For the sample with ZnO–B_2O_3–SiO_2 sol, the dielectric constant (ε_r) varies from 26.7 to 27.3, and the $Q \times f$ value changes from 20,050 to 21,640 GHz. Therefore, the deviation of different pellets in ε_r and $Q \times f$ value was ±0.3 and ±1000 GHz, respectively. However, for the sample with ZnO–B_2O_3–SiO_2 glass, the ε_r changed from 26.5 to 28.0, and the $Q \times f$ value varied from 18,320 to 22,450 GHz. The deviation of different pellets in ε_r and $Q \times f$ value was ±0.8 and ±2100 GHz, respectively. It can be seen that the discreteness of dielectric properties of the ceramic with ZnO–B_2O_3–SiO_2 sol is less than that with ZnO–B_2O_3–SiO_2 glass, resulting from the uniform distribution of ZnO–B_2O_3–SiO_2 sol on the surface of ZnO–TiO_2 powder particles.

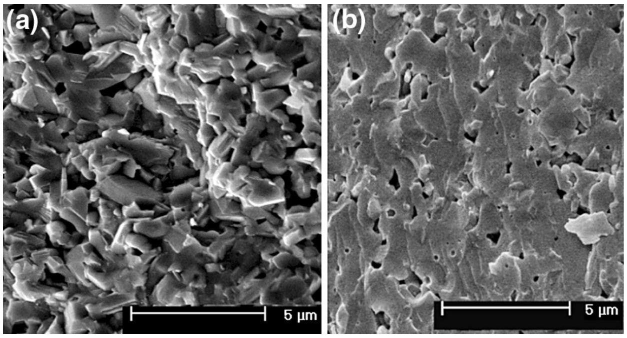

Fig. 5 SEM micrographs of ZnO–TiO_2 samples sintered at 900 °C with **a** ZnO–B_2O_3–SiO_2 sol and **b** ZnO–B_2O_3–SiO_2 glass [19]

2.4 Low-temperature preparation and application of nanoparticles by sol–gel method for electrical contact materials

As core foundation of electrical industry, electrical contact materials and components are responsible for making and breaking a current, and thus, their performance directly determines switching capacity, service life, and reliability of equipment. Environmentally friendly electrical contact materials are attracting more and more attention as the hazardous Ag/CdO material has being phased out in recent years [58–60]. Ag/$La_{0.5}Sr_{0.5}CoO_{3-\delta}$ (Ag/LSCO) is one of the latest environmentally friendly electrical contact materials, in which Ag matrix is strengthened by evenly dispersing LSCO particles. Solid-state reaction is widely used as the synthesis approach of LSCO particles due to its simple process and low cost [61, 62]. However, there exist uncontrolled particles agglomeration, irregular particle sizes, nonuniform compositions, and low phase purity in the solid-state reaction. In this work, we report the low-temperature preparation of LSCO nanoparticles by sol–gel process with inorganic precursors as raw materials for Ag/LSCO electrical contact materials [21–23].

2.4.1 Sol–gel preparation of LSCO nanoparticles

$La_{1-x}Sr_xCoO_{3-\delta}$ ($x = 0.1$–0.7) (LSCO) nanoparticles were successfully prepared by sol–gel with $La(NO_3)_3$, $Sr(NO_3)_2$, and $Co(NO_3)_2 \cdot 6H_2O$ as raw materials. The resultant dried gel is amorphous, the crystalline phase of $La_{1-x}Sr_xCoO_{3-\delta}$ ($x = 0.1$–0.7) is generated after calcined at 700 °C for 8 h (Fig. 6a), and the doping amount does not change the formation of LSCO crystals (Fig. 6b). Compared with solid-state reaction, the formation temperature of $La_{1-x}Sr_xCoO_{3-\delta}$ prepared by sol–gel process is lower than 300 °C. More importantly, the doping of Sr element is easy to achieve in the sol–gel preparation.

2.4.2 Microstructure and electrical conductivity of LSCO nanoparticles

The as-prepared LSCO nanoparticles are spherical, well dispersive, and with smaller particle size (approximately 50 nm) (Fig. 7). As is known, when the size of LSCD particles decreases, the contact area of Ag with LSCD increases correspondingly. A strong adhesion between LSCO and liquid Ag will occur under arc condition, which decreases the splash loss and obtains a high arc erosion

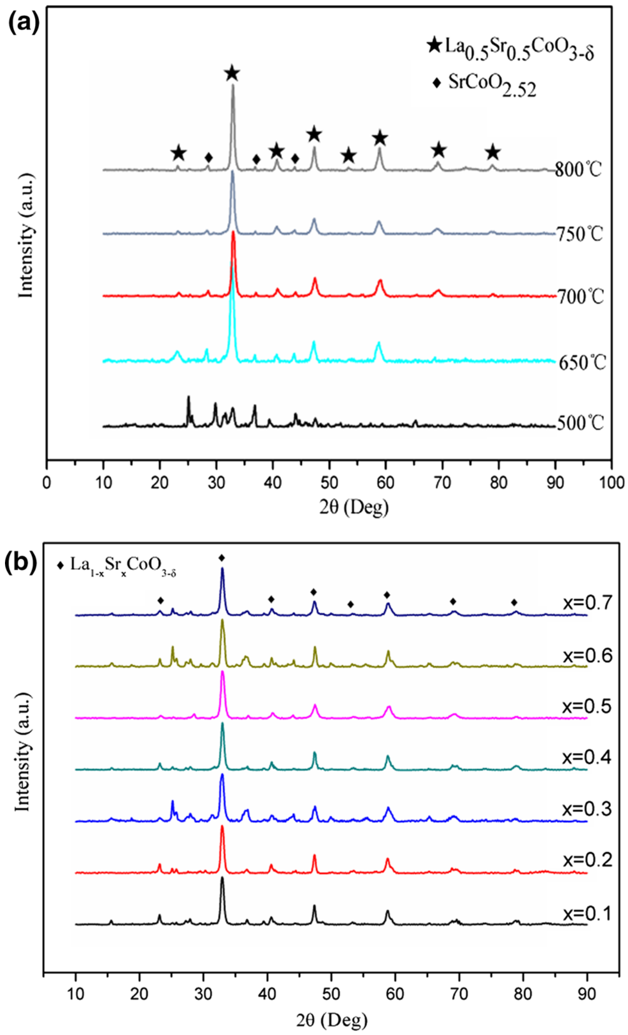

Fig. 6 XRD patterns of LSCO nanoparticles at different temperatures (**a**) and doping concentrations of Sr^{2+} (**b**) [21–23]

resistance. The electrical conductivity of LSCD nanoparticles firstly increases, and then decreases, with the increase in Sr^{2+} doping content. At $x = 0.5$, LSCD nanoparticles have good electrical conductivity ($\lambda_{max} = 5176$ S cm^{-1}). Further increase in Sr^{2+} doping content will obviously decrease the electrical conductivity again.

2.4.3 *Application of LSCO nanoparticles in electrical contact materials*

As shown in Fig. 8a, LSCO nanoparticles prepared by sol–gel method can partially be decomposed in the temperature range of 700–950 °C, while giving off O_2. The emitted oxygen can help to prevent welding and blow out the arc when it occurs in the working process of electrical contact materials, effectively reducing the destruction of the arc on the Ag matrix. The Ag/LSCO electrical contact material was prepared by mechanical alloying process. It

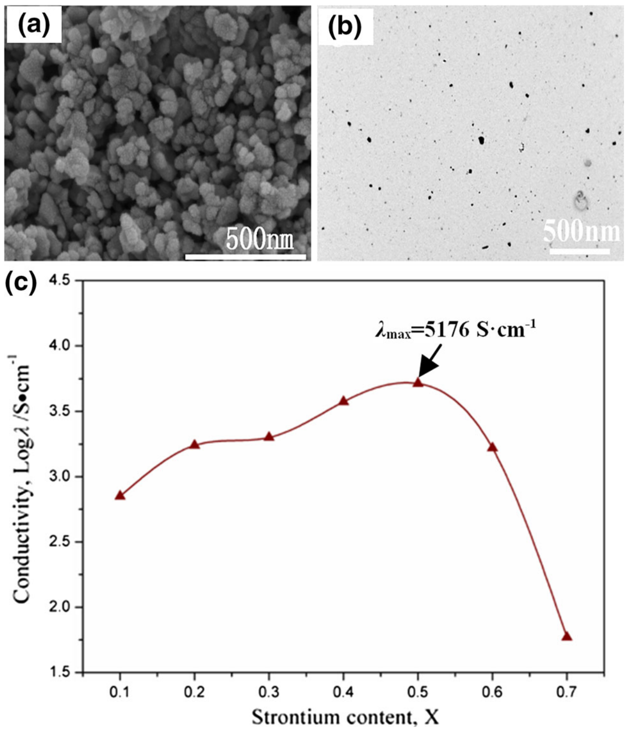

Fig. 7 SEM (**a**) and TEM (**b**) images of LSCO ($x = 0.5$) nanoparticles and conductivity (**c**) of LSCO nanoparticles at different doping concentrations of Sr^{2+} [21–23]

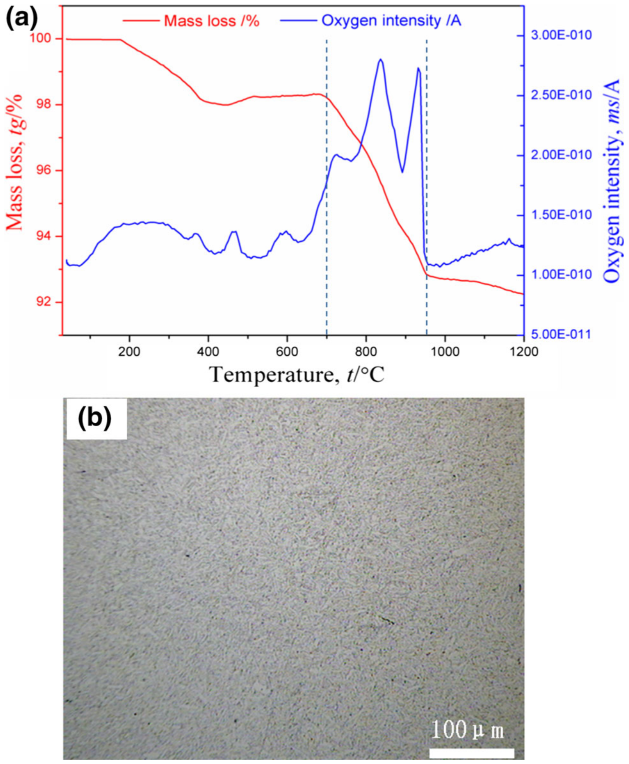

Fig. 8 TG/MS curves **a** of LSCO ($x = 0.5$) nanoparticles and metallographic photograph **b** of LSCO ($x = 0.5$) electrical contact material [21–23]

is seen from Fig. 8b that LSCO nanoparticles uniformly distribute in the Ag matrix, and Ag/LSCO electrical contact material possesses high electrical properties. Summarily, LSCO nanopowders prepared by sol–gel method are more worthy of being chosen as reinforcements in the designing of silver-based eco-friendly electrical contact materials.

2.5 Preparation and application of nanocomposite granules by sol dispersing nanoparticles combining with spray-drying

Dispersion of multiphase nanoparticles is a key factor for the preparation of nanocomposite powder without aggregation, with uniform compositions, and good flowability [63–66]. A uniform and stable suspension (or emulsion) system is known as an important approach to realize the dispersion of multiphase nanoparticles [67–69]. However, it is difficult to achieve the ultimate uniform and stable due to the differences in dispersion mechanism in multiphase nanoparticles with distinctive polarity and isoelectric points. Moreover, the conventional drying technology to obtain nanocomposite powder will change the dispersion and stability of suspension, which leads to the reaggregation of multiphase nanoparticles. Here, the aim of this work was to produce spherical micron-sized nanocomposite granules by sol dispersing nanoparticles combining with aqueous spray-drying. The targeted application for such nanocomposite granules is to prepare SiC-based ceramic nanocomposite [24–26].

2.5.1 Overview of sol dispersing nanoparticles and spray-drying

In the sol dispersing system (Fig. 9a), the $Y_3Al_5O_{12}$ (YAG) sol with fine network is firstly built by sol–gel method, and the size of one network is about 100 nm. About 40-nm β-SiC (87.5 wt%) and 20-nm TiN nanoparticles (2.5 wt%) are added into YAG sol accompanying with dispersant (0.25 wt% dispersant TMAH) in deionized water, and YAG sol and nanoparticles are combined with each other by ball milling. The nanoparticles will be “parceled” or “fixed” by YAG sol, and a network just contains one or two nanoparticles. The sol dispersing nanoparticle slurry system with a 25 wt% solid content has well stability and dispersion by network structure and dispersant.

Spray-drying is an immediate solidifying and drying process, and during spray-drying, the YAG sol is rapidly gelated to form YAG gel with the shrinking of network (Fig. 9b). The shrinking direction of network is to the surface of nanoparticles, and finally, the nanoparticles are absolutely enwrapped by dried network and do not reaggregate each other. Because of this parcel, the nanocomposite powders have a fine distribution after spray granulation.

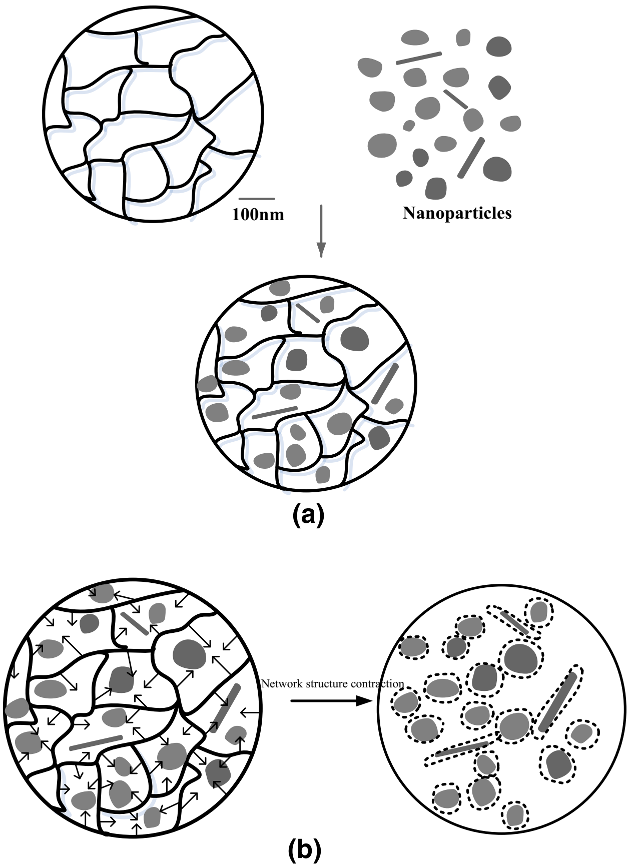

Fig. 9 Construction (**a**) and spray-dry (**b**) models of sol dispersing system [24]

2.5.2 Characteristics of spray-dried nanocomposite granules

Spray-dried granules (Fig. 10a) show spherical pellets with particle size from 10 to 20 μm. The granules have a wide size distribution, indicating good gradation for moulding. From the enlarged surface morphology of a granule, it may be seen that surface structure is smooth without large defects and homogenous chemical compositions, indicating good flowability and compaction properties for green body. The loose density of nano-SiC spray-dried granules reaches to 0.729 g ml^{-1}, and the angle of repose decreases to 26.1°, which confirms that spray-dried granules have well flowability. The distribution of Y, Al, O, Ti, and N in the nanocomposite powders is homogeneous, indicating YAG and nano-TiN uniformly distributing in the matrix (Fig. 10b).

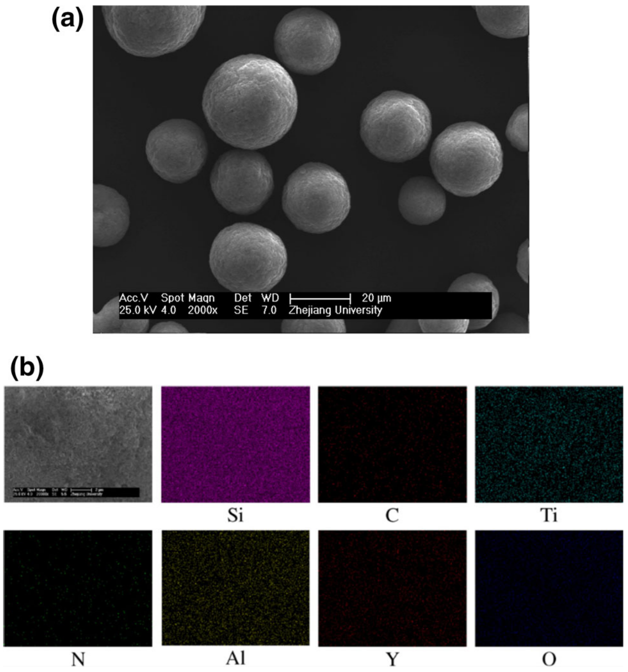

Fig. 10 SEM photograph (**a**) and elemental distribution of surface (**b**) of nano-SiC-based spay-dried granules [24]

2.5.3 *Application of spray-dried granules in ceramic nanocomposites*

The spay-dried nanocomposite granules were uniaxially pressed at a pressure of 160 MPa for 10 s, and cold isostatic pressing with an applied pressure of 250 MPa for 300 s was conducted subsequently. And then, two-step pressureless sintering, that is, after sintered at 1900 °C for 15 min and then 1750 °C for 45 min, was successfully used to densify nano-SiC-based composites. As shown in Fig. 11, the nanocomposites containing 2.5 wt% nano-TiN had high sintering and mechanical properties with relative density of 96.1 %, bending strength of 545.2 MPa, Vickers' hardness of 19.0 GPa, and fracture toughness of 7.8 MPa m$^{1/2}$. The addition of nano-TiN was beneficial to restrain the growth of nano-SiC grains to some extent and obtain uniform microstructure with grain size of 200–400 nm (Fig. 12). The strengthening and toughening mechanism of nano-TiN and YAG grains was integrated to reinforce the nano-SiC-based ceramic composites.

In summary, by combining with sol dispersing nanoparticles and spray-drying, well stability and dispersion of slurry, homogenous distribution and flowability of granules, and nanosized sintering agents for ceramic nanocomposites are obtained simultaneously, which is beneficial for preparing ceramic nanocomposite.

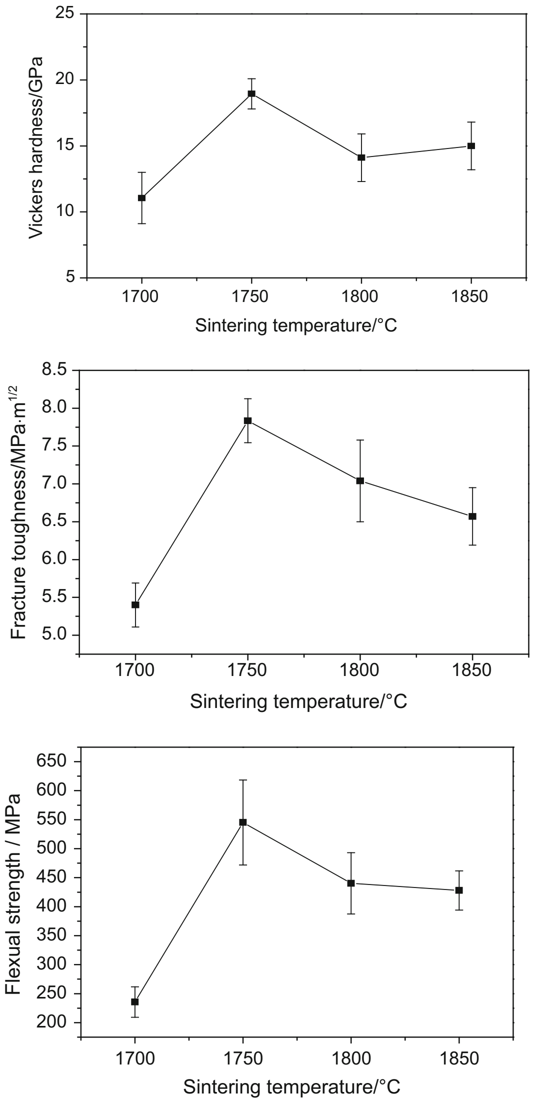

Fig. 11 Mechanical properties of nano-SiC-based nanocomposites as function of sintering temperatures [25]

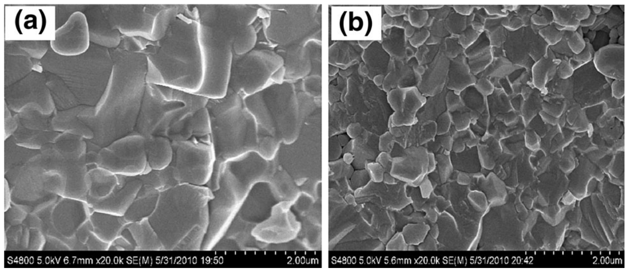

Fig. 12 SEM images of nano-SiC-based nanocomposite sample without (**a**) and with (**b**) 2.5 wt % nano-TiN sintered at 1750 °C [25]

3 The preparation and application of functional coatings by sol–gel technology combining with organic–inorganic hybrid method

3.1 Introduction

Functional coatings have become important advanced materials mainly due to the interesting chemical, optical, mechanical properties. There are several technologies used to deposit functional coatings, such as PVD/CVD (vapor deposition) and the use of a plasma beam, electrochemical deposition, and sol–gel coating technology, wherein sol–gel coating technology is an emerging technology enabling the functional structuration of coatings or thin film due to its well-known advantages (i.e., high-performance, room-temperature, and low-cost process). Sol–gel coating can widely be used as protective, antireflection, medicine, flexible, and antibacterial coatings for various applications such as optics, energy conversion, electronics, or sensing.

Recent development in sol–gel coatings is organic–inorganic hybrid coatings, which are prepared by co-hydrolysis and polycondensation of metal alkoxides or organosilanes and optional organic precursors. The sol–gel-derived hybrid coatings could significantly improve the coating forming process, enhance the microstructure uniformity and functional properties, and extend the application fields that cannot be involved in by sol–gel coatings.

Here, the present work describes an organic–inorganic hybrid method based on sol–gel technology to prepare many kinds of functional coatings such as antireflection coating, anticorrosion coating, wearable coating, and anti-soiling coating [27–31].

3.2 Preparation of organic–inorganic hybrid antireflection coating and its application in solar photovoltaic technology

As solar photovoltaic technology becomes popular as a clean energy technology, the photovoltaic component is widely used. However, the lower conversion efficiency restricts the use of the existing photovoltaic component. Many efforts have been dedicated to improving the conversion efficiency, and the antireflective (AR) coating on solar cover glass is one of the most effective approaches.

Porous silica coating is usually chosen for the AR coating on solar glass of photovoltaic components due to its low refractive index and mechanical stability [70–74]. However, pure inorganic porous silica coating absorbs moisture in air at a high humidity due to the abundant hydroxyl group in the micropore structure of coating, leading to the decrease in the transmittance of the solar glass coated with the AR coating and the conversion efficiency. This is so-called condensation phenomenon. Some solutions to this problem were reported [75, 76]. Guillemot et al. [75] intended to enlarge the diameter of pore structure to reduce the condensation phenomenon on coating, exhibiting the superior condensation resistance performance. Vicente et al. [76] used hydrophobic compound hexamethyldisilazane (HMDS) to modify the coating surface, obtaining the contact angle (CA) in water of 100°.

In the present work [27], the organic–inorganic AR coatings were prepared by a sol–gel method with TX-100 as a porogen and TEOS, MTES as precursors. The effect of the amount of MTES on the properties and structure of coating was investigated, as shown in Fig. 13. The transmittance of coating is low in the absence of MTES (see bare glass in Fig. 13). The transmittance of AR coating increases in the presence of MTES, and the maximum transmittance is 99.6 % at 530 nm when the ratio of MTES to TEOS is 1:2. The surface of AR coating becomes rougher when MTES increases. The more mesopore structure with the pore diameter of 30 nm appears in the coating when the amount of MTES increases, as shown in Fig. 14. The decrease in the abrasion resistance of the coating leads to the increase in the average transmittance. The optimum performance of AR coating can be obtained at the mole ratio of MTES to TEOS of 1:2.

3.3 Preparation of organic–inorganic hybrid anticorrosion coating and its application in metal protection

Metals are extensively used in many industrial fields, and their surfaces are generally protected by various coatings to avoid corrosion. Traditionally, chromate coatings are of the most effective and economical corrosion protection coatings [77]. However, the chromates, especially Cr^{6+}, are toxic and will be eliminated in the industrial products in the near future. So the substitution for the chromate

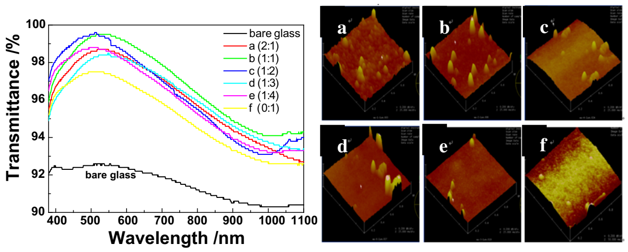

Fig. 13 Transmittance and SPM images of AR coatings with different mole ratios of MTES to TEOS [27]

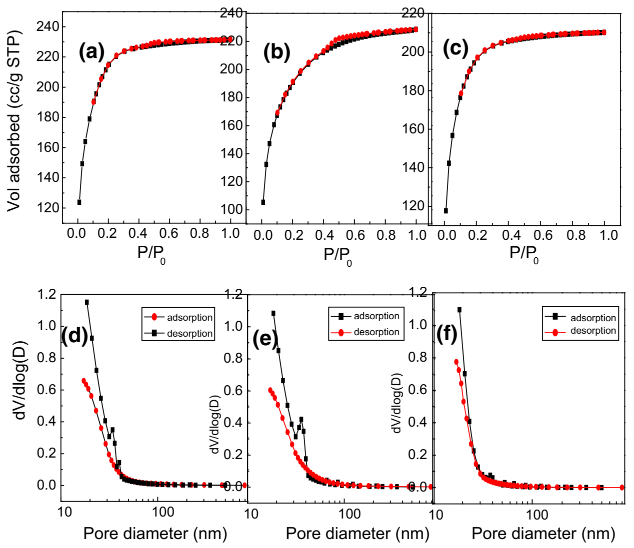

Fig. 14 Nitrogen adsorption–desorption isotherms (**a**, **b**, **c**) and *t*-plot diagram (**d**, **e**, **f**) of the powders from AR coating solution with different amounts of MTES. **a**, **d** MTES:TEOS = 2:1, **b**, **e** MTES:TEOS = 1:2, **c**, **f** MTES:TEOS = 0. (the *black symbols* represent adsorption curves, the *red symbols* represent desorption.) [27]

anticorrosion system becomes a popular topic in the material research areas. One of the prospective substitutes for the chromate anticorrosion system is sol–gel-derived films. Most recently, many studies have been carried out and have made some progress [78, 79], and various kinds of modified silicon alkoxide (ORMOSIL)-derived anticorrosion coating and their anticorrosion performance were studied [80, 81]. However, regarding the application of coatings, besides anticorrosion, other properties such as heat resistance and wear resistance need to be investigated as well. Furthermore, the performance of anticorrosion for the sol–gel films still needs to be improved.

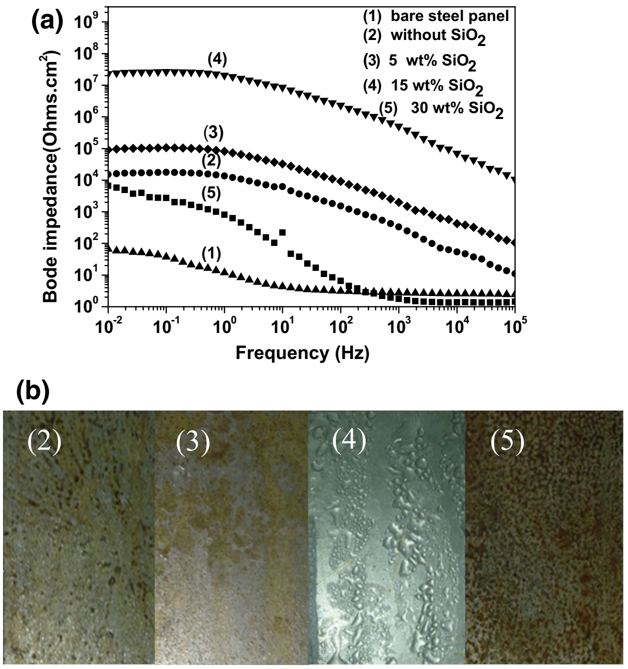

Fig. 15 Bode impedance plot and photographs of uncoated and coated cold rolled steel panel in 3.5 % NaCl solution: (*1*) bare cold rolled steel panel; (*2*) without SiO$_2$ nanoparticles; (*3*) coating loaded 5 % SiO$_2$ nanoparticles; (*4*) coating loaded 15 % SiO$_2$ nanoparticles; (*5*) coating loaded 30 % SiO$_2$ nanoparticles [28]. **a** EIS behavior of hybrid coatings. **b** Photographs of hybrid coatings after 96 h of salt spray tests

In our early work, methyl triethoxysilane (MTES) and tetraethoxysilane (TEOS) were used as precursors to produce the anticorrosive coatings with organic–inorganic compound, but the anticorrosion performances of the coating are unsatisfied [82]. So, by using SiO$_2$ sol as the source of nanophase and MTES as the precursor, a SiO$_2$/polysiloxane hybrid coating for anticorrosion was prepared by sol–gel technique. The effect of SiO$_2$ nanoparticles on the properties and structure of coatings were studied [28]. From Fig. 15, compared with bare cold rolled steel panel (curve 1 in Fig. 15), the impedance magnitude of the coated steel panel increases greatly. For hybrid coatings, when the amount of SiO$_2$ nanoparticles increases from 0 to 15 wt%, the anticorrosion performance of coating increases and the impedance magnitude reaches maximum at 15 %. It is possibly because that the used SiO$_2$ nanoparticles increase the interfaces between SiO$_2$ and the polysiloxane matrix compared with micron SiO$_2$ particle. With further increasing the amount of SiO$_2$ nanoparticles to 30 wt%, the impedance magnitude drops sharply (curve 5) which is even lower than the undoped coating (curve 2), especially in high-frequency range. The photographs of the hybrid coatings with different amounts of SiO$_2$ nanoparticles are consistent with electrochemical impedance spectra (EIS) measurements.

The texture (Fig. 16a) of coating without SiO$_2$ is uniform and even, and the roughness of coating texture increases with the doping of SiO$_2$ nanoparticles, especially for the doping of 30 wt% SiO$_2$ nanoparticles, which results in the segregation of nanoparticle phase and the polysiloxane matrix. The segregation will destroy the compactness of the hybrid coating and finally results in deterioration of the barrier properties or anticorrosion performance of the coatings. The DTA curves (Fig. 16b) show that with the doping of SiO$_2$ nanoparticles, the exothermic peaks of hybrid coatings become smaller and shift to the higher temperature, resulting from high temperature of decomposition of methyl group from MTES. This result suggests that SiO$_2$ nanoparticles doping can also improve the heat resistance of the hybrid coating by several decades centigrade.

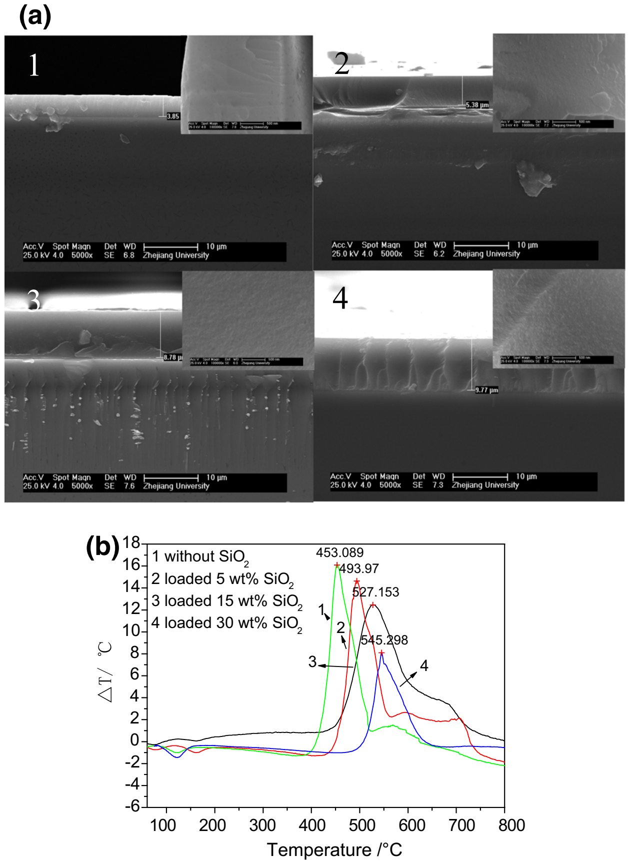

Fig. 16 SEM photographs and DTA curves of hybrid coatings with different amounts of SiO_2 nanoparticles: *1*—without SiO_2; *2*—5 wt% SiO_2 sol; *3*—15 wt% SiO_2 sol; *4*—30wt % SiO_2 sol [28]. **a** SEM photographs of hybrid coatings. **b** DTA curves of hybrid coatings

3.4 Preparation of organic–inorganic hybrid wearable coating and its application in surface reinforcing of optical plastics

Optical plastics such as polycarbonate (PC) are a kind of the most widely used engineering thermoplastics because of transparency, excellent toughness, thermal stability, and a very good dimensional stability and have been gradually replaced inorganic glass in application for shatterproof windows, lightweight eyeglass lenses, and optical devices. However, optical plastic is easy to be scratched in use due to the low surface hardness and poor wear resistance, which makes the loss of operation life and limits the application. One of the effective methods to improve the properties of optical plastics such as surface hardness, abrasion resistance, and transparency is to spread hard film or coating on it. At present, the hard film includes three types: inorganic film, organic film, and inorganic–organic film. The inorganic film has high hardness but poor adhesive to organic substrates. The organic film adheres to organic substrates strongly, but the hardness is poor. The organic–inorganic film can integrate the excellent properties of the organic phase and of the inorganic phase into one materials and yield the properties of high abrasion resistance, high transparency, and good adhesion, which has became the hot study spot of abrasion-resistant coatings on optical plastics [83–86].

In the present work, on the basis of present research of organic silicone films, the inorganic sol modified silicone hybrid wearable coating was prepared by sol–gel method. The composition, structure, and properties of the resultant hybrid wearable coating were studied systemically [29–31]. Firstly, the ethylorthosilicate, aluminum isopropoxide, and zirconium oxychloride were hydrolyzed and condensed in mixture of alcohol and water and aggregated to nanosized silica, alumina, and zirconia sol particles. Secondly, with KH-570 modified silica, alumina, and zirconia as inorganic phase, condensates of methyltrimethoxysilane (MTMS) as film forming materials, the modified sol/silicone hybrid wearable coating was prepared on PC, respectively. The hybrid wearable coating is composed of inorganic network structure such as Si–O–Si,Si–O–Al,Al–O–Al,Si–O–Zr, and Zr–O–Zr endcapped with organic groups, and the addition of KH-570 can improve the stability of coating solution, and the flexibility of coating because of the long alkyl chain. As a result, the sol/organosilicone hybrid coating with crack-free, adjustable thickness, wear resistance, and high light transmittance can be obtained, as show in Figs. 17, 18, and 19.

The silica sol enhancing silicone hybrid coating improves the light transmittance and hardness of PC. When

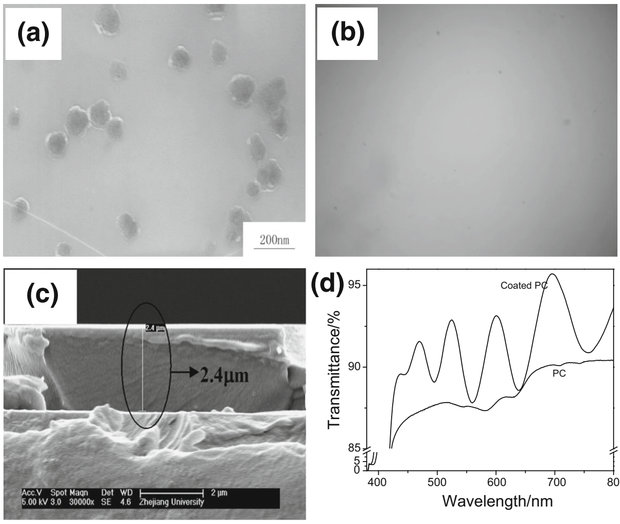

Fig. 17 TEM photograph of silica sol/organosilicone hybrid coating solution, metallographic microscope photograph of silica sol/organosilicone hybrid coating (×50), SEM images of cross section of coating, and transmittance of coated PC [29]

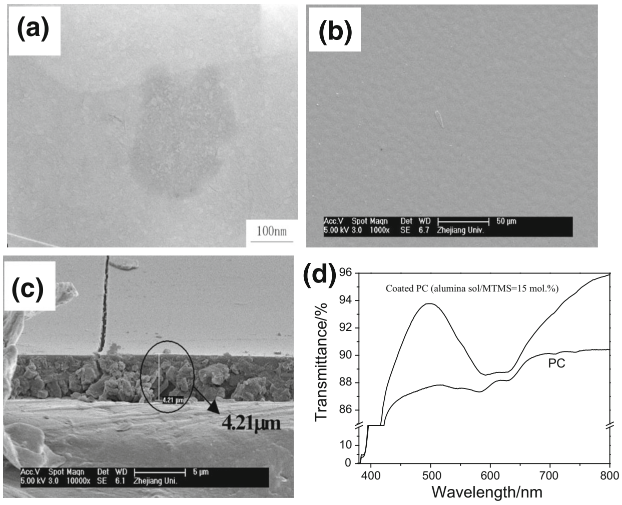

Fig. 18 TEM images (**a**) of alumina sol/organosilicone hybrid coating solution, SEM images of surface (**b**) and cross-section (**c**) of alumina sol/organosilicone hybrid coating, and transmittance (**d**) of coated PC [29]

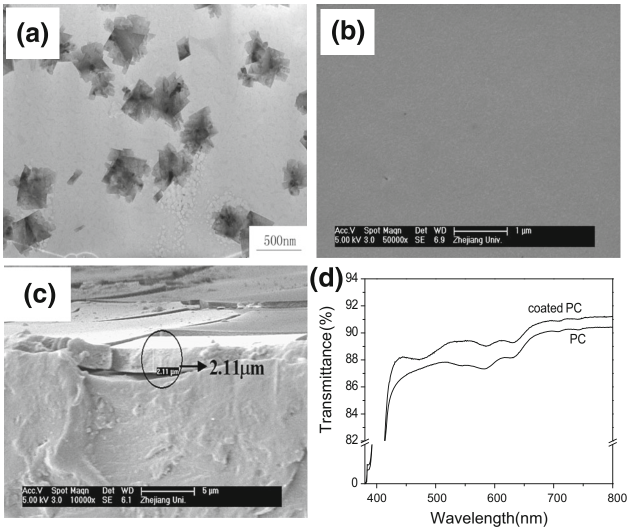

Fig. 19 TEM images (**a**) of zirconia sol/organosilicone hybrid coating solution, SEM images of surface (**b**) and cross-section (**c**) of zirconia sol/organosilicone hybrid coating, and transmittance (**d**) of coated PC [31]

mole ratio of TEOS and MTMS was 2, the pencil hardness of PC was improved from 2B to 2H, and the light transmittance of silica sol/organosilicone hybrid-coated PC was increased from 88.6 % to above 90 %. Alumina sol was more effective to increase hardness than silica sol. When the mole percent of Al and MTMS was 15 %, the pencil hardness of alumina sol/organosilicone hybrid-coated PC reached 2H, and the light transmittance of the coated PC was above 90 %. The effect of zirconia sol/organosilicone hybrid coating on light property of PC changed with zirconia sol content. When mol ratio of Zr and Si was lower than 1, the light transmittance of zirconia sol/organosilicone hybrid-coated PC was above 88.6 %, while the highest pencil hardness of the coated PC is only H.

It is of important theoretical value and instructive meanings to the research and development of hybrid wearable coating prepared by sol–gel method and the surface modification and extant application of optical plastics.

3.5 Preparation and super-hydrophobic properties of lotus-leaf-like hydrophobic antibacterial film

Bacteria have a strong ability to attach to solid surfaces and finally form a biofilm, which will serve as a reservoir for the development of pathogens, leading to health threats of mankind. Biofilm formation is a multifactorial infection process, which is also influenced by the physiochemical properties of the substrate surface. It has been reported that hydrophilic surface is a major factor for bacterial adhesion and biofilm, while hydrophobic surface can effectively inhibit protein adsorption and bacterial adhesion on materials [87–90]. However, it is difficult to obtain notable hydrophobicity surface just relying on the low surface energy, especially for so-called lotus effect surface. The observation of hydrophobicity related to the topology of the surface of a plant leaf was reported by Barthlott and Neinhuis [91]. It was believed that this unique property is based on surface roughness caused by the micrometer-scale papillae and the epicuticular wax [92]. Jiang also reported a novel finding of lotus leaf, i.e., branch-like nanostructures on top of the micropapillae [93]. These structures can induce super-hydrophobic surfaces with large water contact angle, as well as high bacteriostatic ability. However, resisting bacteria via the super-hydrophobic surface is only a kind of passive strategies, because the super-hydrophobic surface just reduces bacterial adhesion rather than kills them. More importantly, the bacteria will still adhere to the super-hydrophobic surface when the surface becomes fully wet after long time exposing to moist environments [94, 95]. Thus, more and more attentions are paid on the combination of super-hydrophobic surface and bacterial killing materials [96, 97].

In the present work, we report a novel method to fabricate a lotus-leaf-like hydrophobic antibacterial film via three-step process (see Scheme 1). Firstly, Ag^+ ions are adsorbed on the surface of sulfonated polystyrene (PS) beads via electrostatic interaction, and then reduced and protected by polyvinylpyrrolidone (PVP) to obtain PS/Ag composite spheres. Secondly, silica colloids generated by the hydrolysis and polymerization of tetraethoxysilane (TEOS) are assembled on the PS/Ag composite spheres via hydrogen bond force to form silica shell, followed by the

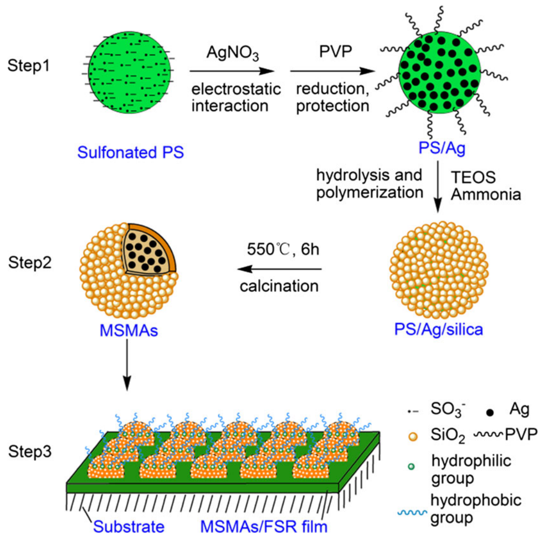

Scheme 1 Schematic diagram of the three-step processes to fabricate a lotus-leaf-like hydrophobic antibacterial film [32]

removal of the PS core and PVP through calcinations to get MSMAs. The obtained MSMAs (Fig. 20a) possess relatively uniform shape with rough surface, whereas at the inner of the hollow microcapsules, it can be seen that many AgNPs, corresponding to the white spots, load onto the interior wall of the spherical shell (Fig. 20b). More importantly, the Ag^+ ions can release from AgNPs via oxidization by dissolved oxygen and slowly diffuse to the external medium through the mesopore channels in the shell, inducing sustained-release property and antibacterial activity. Thirdly, the MSMAs are loaded onto the FSR (fluorosilicone resin) film, and the silanols on the silica colloid surfaces provide bonding site, leading to combination with FSR molecular chains, which allows the MSMAs to be partially embedded in the film (see Fig. 21a), forming a lotus-leaf-like hierarchical microscale- and nanoscale-structured surface. Therefore, the hydrophobicity of MSMA/FSR film is enhanced, and its water contact angle increases from 112.0° (FSR film) to 150.4°. The MSMAs/FSR film displays higher antibacterial activity compared with FSR film, indicating that the high antibacterial activity can be achieved by the joint action of the super-hydrophobic property and the sustained release of Ag^+ ions.

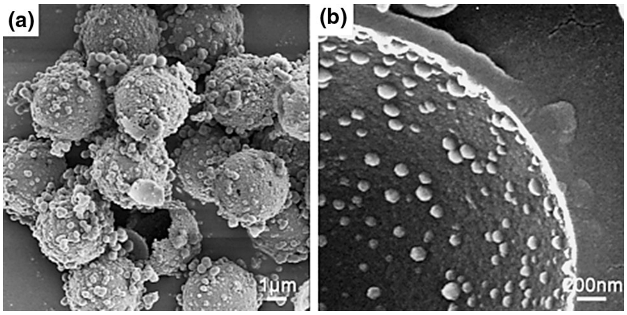

Fig. 20 Electron microscope images of MSMAs: **a** SEM image; **b** SEM image of cross section of the MSMAs [32]

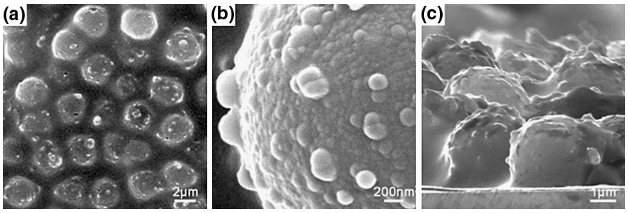

Fig. 21 SEM images of **a**, **b** the MSMAs/FSR film in different magnification; **c** the cross-sectional structure of the film [32]

4 The fabrication and application of hollow microspheres by sol–gel route combining with self-assembly technology or emulsion process

4.1 Introduction

Hollow microspheres are all kinds of the core–shell-structured microspheres with the internal hollow structures such as simple cavity structure, multicavitiy structures, multishell hollow structure, and sandwich hollow structure. Increasing attention has been attracted by hollow microspheres due to their special characteristics, such as low density, low thermal conductivity, high specific surface, and good flow ability. Hollow microspheres have been widely used in all kinds of applications such as catalysis, adsorption, drug delivery, and building materials [98].

Up to now, diverse hollow microspheres with different special characteristics including hollow microspheres with a single cavity, hollow microspheres with multiple shells, and hollow microsphere with multicavities have been fabricated by templating method, emulsion processing, high-temperature treatment, layer-by-layer self-assembly technique, and so on, wherein hollow microspheres with multicavitiy pores as an important class of hollow spheres have gained growing attention for their potential applications such as adsorption and catalysis, especially in drug delivery systems. Moreover, the microspheres loaded with nanoparticles and mesoporous-structured shell have been also fabricated for multiple applications, such as light diffusers and magnetic-assisted separation agents.

Here, we demonstrate the preparation and nanoparticle loadings of some typical hollow mesostructured microspheres by sol–gel route combining with self-assembly technology or emulsion process as follows [35–40].

4.2 Preparation of novel mesoporous silica hollow microspheres inside-loaded Ag nanoparticles by sol–gel self-assembly technology

Ag nanoparticles (AgNPs) have shown more superior antibacterial activity compared to that of bulk silver as well as other silver compounds [99–101], due to their high specific surface area, high fraction of surface atoms, and broad-spectrum antibacterial activity [102, 103]. However, AgNPs, with the form of colloids, have tend to aggregate in practical application as their high surface activity, leading to the deterioration of chemical properties and antibacterial performance [104, 105]. Moreover, another problem encountered in the antibacterial application of AgNPs is that antibacterial materials are desired to be chemically durable, and to release Ag slowly over a long period [103].

One of the strategies for overcoming above problems is to load AgNPs on supporting matrix. Various kinds of AgNP-loaded antibacterial materials have been developed in the past decades. These investigations mainly focused on the deposition of AgNPs on inorganic microspheres (silica, titanium dioxide, carbon spheres, etc.) [106–108], nanofiber or nanotube (titanium dioxide or carbon) [109–111], polymer films (polystyrene, carboxymethyl-chitosan, polyamide, etc.) [112–115]. However, in all these researches, AgNPs were just loaded on the surface of matrix and thus may be quickly consumed due to the weak binding, chemical erosion or excessive extraction, resulting in rapid decrease in antibacterial activity. Hence, sustained-release performance of AgNP-loaded composite materials is required considering the practical application. Some efforts have been made toward the development of core–shell system to isolate the inner AgNPs core from the outer environment [116–118]. In the typical preparation process, AgNPs were used as cores, and silica was directly coated on the AgNPs through a modified Stöber method to provide a robust substrate with consistent surface chemistry. This core–shell structure can effectively protect active AgNPs and solve the oxidation problems, and thus achieve relatively high chemical stability. However, the current researches of such core–shell Ag–silica composite material mainly focus on its application in optical fields, such as SERS or nonlinear optical response, while rarely discuss its antibacterial performance [116–118]. For the antibacterial application of such core–shell Ag–silica composite material, it is believed that the potent antibacterial ability of the AgNPs cannot be put into full play in this core–shell structure, due to its slow Ag ions release rate [119], and thus how the Ag^+ ions release from the core–shell structure is still a challenging problem. Hence, it is necessary to design a new form of Ag–silica composite structure, to get better antibacterial performance.

Herein, we report a sol–gel method to fabricate mesoporous silica microcapsule with AgNPs loading onto the interior wall of mesoporous silica shell (denoted as AgNPs@silica microcapsule) [33, 34]. The preparation mechanism of AgNPs@silica microcapsule is illustrated in Fig. 22a. Firstly, sulfate groups are introduced at the surface of PS beads via sulfonation to obtain negative charged sulfonated PS beads, and then Ag^+ ions will be adsorbed on the surface of sulfonated PS beads via electrostatic attraction after addition of silver nitrate ($AgNO_3$).

Secondly, PVP serving as both reducing and protecting agent is added to the reaction system. PVP macromolecule in solution which mostly likely adopts a pseudo-random coil configuration may take part in some form of association with the metal atoms, thus increasing the probability of nucleus formation. More specifically, Ag^+ ions will coordinate with lone pair electrons from the oxygen (O) and nitrogen (N) atoms of polar groups (O=C–N) in PVP molecules, and the polar group of one PVP unit may

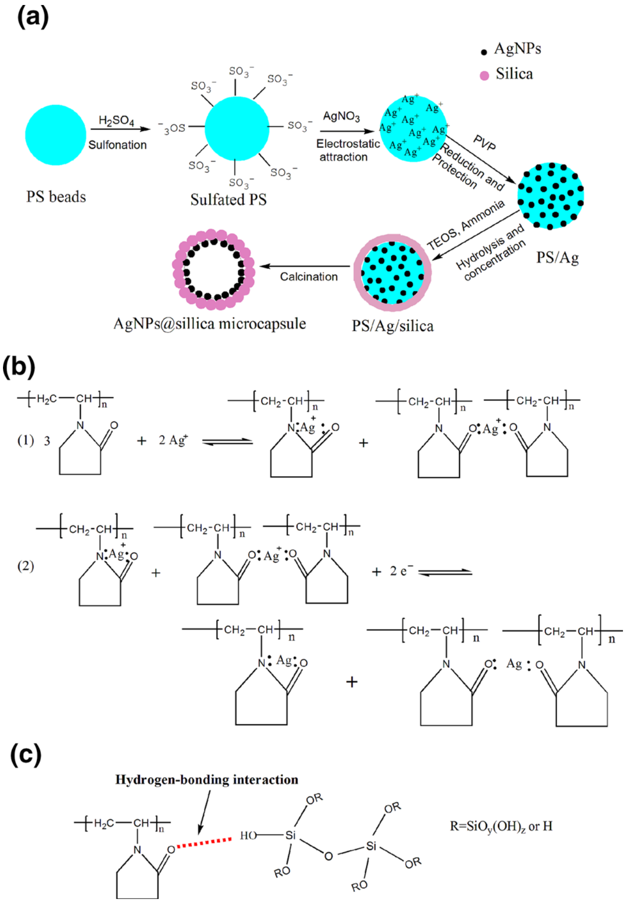

Fig. 22 Schematic illustration of the forming mechanism of AgNPs@silica microcapsule [33]. **a** Preparation mechanism of AgNP@sillica microcapsule. **b** The reduction and protection mechanism of PVP. **c** The combination of silica and PVP molecules

occupy two *sp* orbitals of the Ag^+ ions to form a complex compound [29, 30] (as shown in Fig. 22b). Thus, the coordination structure is activated, and the Ag^+ ions in the coordination compounds may receive electronic clouds from the ligand of –N and O=C in pyrrolidone ring to form Ag nuclei atomic metal that grow into AgNPs, resulting in the formation of PS/Ag composite spheres [120]. Thirdly, silica colloids (primary particles, several nanometers), generated by the hydrolysis and concentration of tetraethoxysilane (TEOS) with the catalysis of ammonia, are assembled on these spheres to form core–shell PS/Ag/silica composite spheres. The silanols (Si–OH groups) on the silica colloid surface provide bonding site, and will combine with PVP molecular chains via hydrogen bonding force between OH- and O atom on the carbonyl group (C=O), as shown in Fig. 22c, thus achieving order assembly of silica shell, whereas PVP molecules will also be trapped in the structure of silica shell due to hydrogen bonding combination [121]. Finally, the PS core and PVP are removed by calcinations, forming AgNPs@silica microcapsule characterized by hollow core and mesoporous shell with AgNPs loading onto the interior wall.

It can be seen from the typical SEM images of PS beads (Fig. 23a) that the PS beads are uniform with a diameter of ca. 3 μm and have good monodispersity. As shown in Fig. 23b, AgNPs reduced by PVP are homogenously supported on the surfaces of PS beads without any aggregation. The diameter of the monodispersed Ag NPs is about 90 nm, as seen inset in Fig. 23b. In order to observe the interior wall of the silica shell, the microcapsule was dispersed into ethanol and ultrasonized to get broken spherical shells. As shown in Fig. 23c, it can be seen that many AgNPs, corresponding to the white spots, load onto the interior wall of the spherical shell, which is in well consistence with Fig. 23b. Moreover, it can be also observed from the edge of broken spherical shell that the thickness of the shell is about 100 nm, and the shell is composed of monolayer of silica particles.

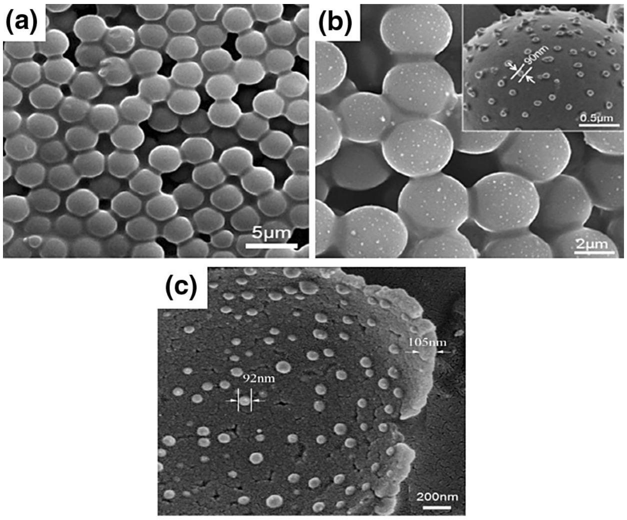

Fig. 23 SEM images of **a** PS beads; **b** PS/Ag composite spheres, the inset is a magnified SEM image; **c** SEM image of a broken microcapsule [33]

As shown in Fig. 24a, the concentration of Ag released from the interior of the shell into water increases with soaking time and reaches the equilibrium after 6 days. Figure 24b gives a distinct picture of the release rate of Ag. It displays a three-stage release profile characterized by an initial rapid release phase, followed by a modulated and progressive release of Ag for several days, and then reaches approximately dynamic equilibrium at last. It indicates that the AgNPs@silica microcapsule can protect the immobilized AgNPs for a long time. Therefore, the antibacterial activity of AgNPs@silica microcapsules can remain at a high level of 99.2 % (as shown in Table 2), even being soaked into deionized water for 2 months, further proving that the as-prepared AgNPs@silica microcapsule can release Ag slowly and maintain their high antibacterial activity for long periods.

This unique structure can protect the inner AgNPs and effectively avoid the aggregation problem existing in traditional Ag colloid system, keeping the inherent activity of individual AgNPs. Meanwhile, owing to the mesoporous structure of the shell, Ag^+ ions can be slowly released from the interior of the shell, resulting in higher antibacterial durability.

4.3 Template-free synthesis of three-dimensional mesoporous nanocomposite microspheres

The photocatalytic activity of semiconductor materials mainly depends on the specific surface area, light response characteristic, and quantum efficiency [122–125]. Thus, with respect to the bulk materials, nanoscale photocatalytic materials often exhibit better catalytic activity due to their larger specific surface area and higher quantum efficiency [126]. However, there are difficulties in dispersing the nanoscale materials and recycling them from the solutions. In recent years, 3D micro- and nano-hierarchical structure

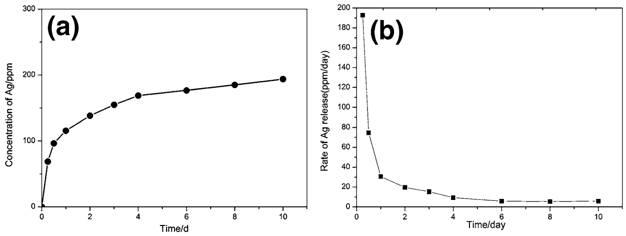

Fig. 24 Concentrations of Ag released from the interior of the AgNPs@silica microcapsule into water with various soaking time (**a**); release rate of Ag with various soaking time (**b**) [33]

Table 2 Antibacterial test results against *E. coli* [33]

Test time	Sample	Number of remaining colonies($\times 10^3$ cell/ml)	Reduction in *E. coli*
Initial	Pure silica powders	573	–
	AgNPs@silica	1	99.8 %
After 2 months	Pure silica powders	612	–
	AgNPs@silica	5	99.2 %

materials, which are assembled from nanoparticles, nanorods, nanoplates, and other building blocks, have attracted significant attention due to their unique morphology and properties [127–129]. A large number of studies have shown that this kind of three-dimensional micro- and nano-structural materials can effectively overcome the above problems and usually exhibit superior photocatalytic properties [130–134].

In this work, 3D hierarchical structure $InVO_4$ porous microspheres with different grain size and morphology was successfully synthesized by a sol–gel method under hydrothermal conditions in the presence of cetyltrimethylammonium bromide (CTAB) [34, 35]. The most plausible mechanism for the growth of the monodisperse microspheres can be proposed to include Oswald ripening and self-assembly aggregation, as shown in Fig. 25. Firstly, numerous small crystallites nucleate from solution, and the primary amorphous nanoparticles quickly suffer from entropy-driven random aggregation, and the growth of crystallites results in the formation of well-crystallized $InVO_4$ nanoparticles through the typical Oswald ripening process [135–137] (Step 1). Secondly, the self-random aggregation of $InVO_4$ nanocrystals, which have a higher surface energy, will assemble spontaneously to form perfect hierarchical microspheres in order to further reduce the interfacial energy [138, 139] (Steps 2 and 3). From a view of kinetics, however, for the aggregates to form perfect spheres, there must be sufficient short-range repulsion due to surface charge between them to allow the particles to settle into the microspheres in addition to high concentration of primary particles [140]. So, the cationic CTAB template here is important as expected to bind the nanoparticles together through electrostatic interaction after the aggregation has taken place.

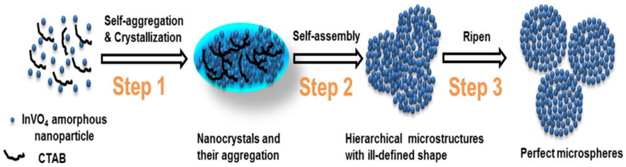

Fig. 25 Formation mechanism of $InVO_4$ 3D micro- and nanohierarchical microspheres [34]

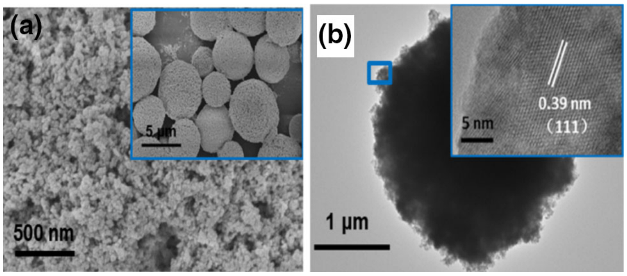

Fig. 26 SEM image (**a**) and TEM image of 3D micro- and nanohierarchical microspheres. The *inset* of (**a**) is the corresponding image of low magnification; the *inset* of (**b**) is the corresponding image of high magnification [34]

As shown in Fig. 26a, the $InVO_4$ nanoparticles assemble spontaneously to form hierarchical microspheres with the diameter about 2–5 μm. Figure 26b shows a single $InVO_4$ microsphere with 3D hierarchical structure composed of small-size particles. The inset of Fig. 26b shows clear lattice fringes with the lattice interplanar spacing of 0.39 nm, which corresponds to the (111) crystalline plane of orthorhombic $InVO_4$.

Furthermore, we further fabricated $TiO_2/InVO_4$ nanocomposites based on the in situ growth of TiO_2 nanoparticles on 3D hierarchical $InVO_4$ porous microspheres, as shown in Figs. 27 and 28 [35]. Such structural material offers two advantages: (1) TiO_2 nanoparticles can be uniformly loaded on the surface of $InVO_4$, forming interconnected biphase $TiO_2/InVO_4$ nanocomposites with the close interface, which leads to the highly efficient interparticle electron transfer and thus achieving improved

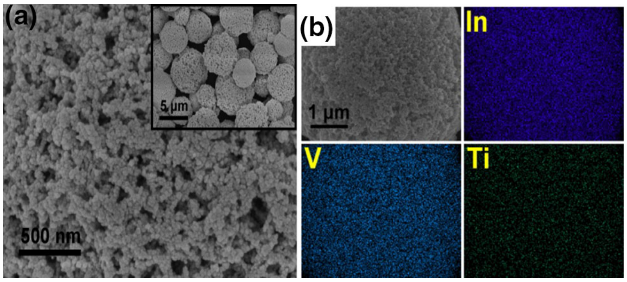

Fig. 27 SEM image (**a**) and SEM–EDS mapping data (**b**) of $TiO_2/InVO_4$ nanocomposites. The *inset* is the corresponding image of low magnification [35]

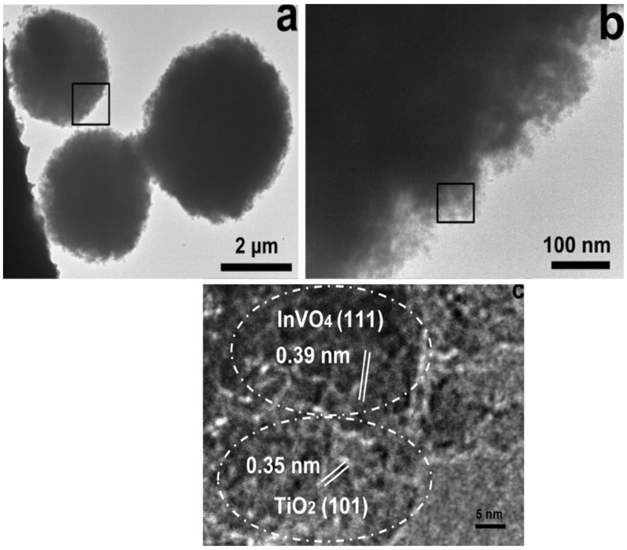

Fig. 28 TEM (**a**, **b**) and HRTEM (**c**) images of $TiO_2/InVO_4$ nanocomposites [35]

photocatalytic properties [141]; (2) The 3D hierarchical porous microspheres can combine the advantages of high-surface-area materials and large-scale materials, achieving both high photocatalytic activity and easy recycling characteristics, thereby showing a promising potential in environmental protection.

4.4 Fabrication of metallic oxide hollow microspheres with incontinuous multicavities by oil–water (O/W) emulsion process accompanied by sol–gel reaction

Metallic oxide hollow microspheres possess excellent characteristics derived from metallic compositions and hollow structure simultaneously, such as good thermal stability, chemical stability, electrical conductivity, low density, and high porosity [142–144]. Due to the unique characteristics, metallic oxide hollow microspheres have a wide range of applications in the sensitive material, biochemistry, solid oxide fuel cell, thermal barrier coatings, etc. [145–149]. In this work, typical metallic oxides such as TiO_2, ZrO_2, and Al_2O_3 have been successfully prepared via an oil–water (O/W) emulsion process accompanied by sol–gel reaction in the presence of polyvinylpyrrolidone (PVP), without any templates at room temperature [36–39].

4.4.1 Formation mechanism of hollow microspheres with multicavities

The mechanism for the formation of the TiO_2 hollow spheres with multicavities may be explained on the basis of nucleation-growth phase separation model, which is schematically shown in Fig. 29. The oil phase is cut into small spherical droplets by high-speed shearing under vigorously stirring when it is mixed with water phase. Then, the water molecules diffuse through oil–water interface and react with tetrabutyl titanate. The reaction is comprised of the hydrolysis of tetrabutyl titanate and polycondensation, leading to the sol–gel transition of the original oil droplets which built the solid spheres. The addition of EAA suppresses the hydrolysis of tetrabutyl titanate, which ensures the thoroughly emulsification of oil phase before gelation to form spherical morphology. And the PVP acted as phase separation agent in this reaction is crucial in the formation of porous structure of TiO_2 microspheres. Moreover, Span 80 used as phase separation stabilizer has a great effect on the preservation of spherical morphology and porous structure of TiO_2 microspheres.

4.4.2 Control of multicavity structures inside hollow microspheres

As shown from the SEM images of TiO_2 microspheres fabricated with different amounts of PVP (Fig. 30), spherical structures are obtained for all five particles, and the surfaces of the microspheres fabricated with different amounts of PVP are generally smooth. The addition of PVP leads to cage-like porous structures, and the average cavity diameters calculated from the SEM images are ~500 nm, ~750 nm, ~1.2 μm, and ~1.3 μm, respectively, as shown in Fig. 31. It indicates that the cavity size distributions also become wider with the increase in PVP content generally. However, the addition of PVP nearly does not affect the size distribution of titania microspheres, and all the samples show a size distribution with only one peak.

4.4.3 Preparation of other metallic oxides hollow microspheres by using similar approach

As known, hollow zirconia and alumina spheres are widely used as absorbents, composite materials, ceramics, and catalyst support due to their instinct microporous structures, large surface area, high stability, and various acid/basic sites. Herein, the one-step route presented in this

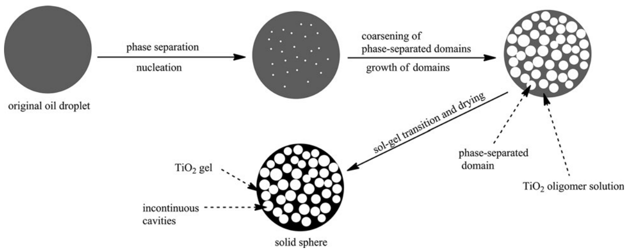

Fig. 29 Illustrative mechanism for the formation of hollow microspheres with multicavities [36]

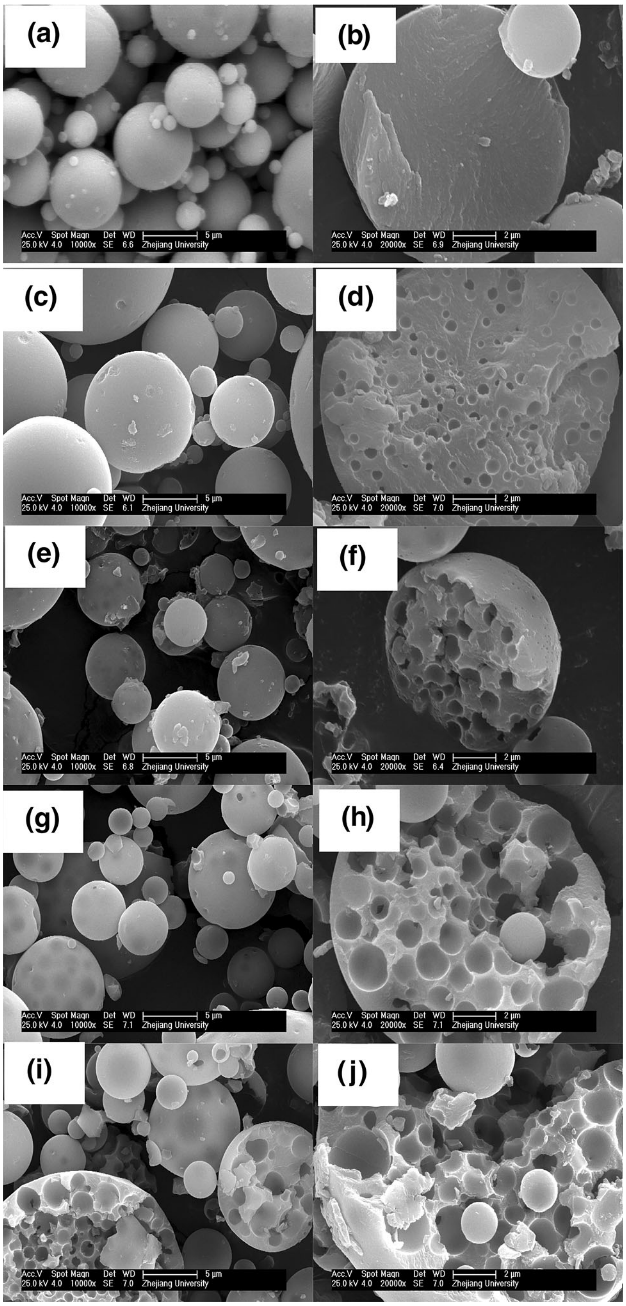

Fig. 30 SEM images of the titania microspheres with different PVP contents [36]

work is proven to be applicable to fabricate zirconia and alumina microspheres with incontinuous multicavities successfully, as shown in Fig. 32.

4.5 Synthesis of porous ethyl cellulose (EC) microspheres loaded with nanoparticles by oil-in-water (O/W) emulsion process

Ethyl cellulose porous spheres (ECPSs) as an important class of hollow spheres have gained growing attention for its potential application in drug delivery system because of high porosity, nontoxicity, good mechanical properties, and other advantages [150–153]. Moreover, the hollow spheres loaded with nanoparticles have also been fabricated for multiple applications, such as light diffusers and magnetic-assisted separation agents [154]. In this work, ethyl cellulose porous spheres (ECPSs) loaded with various amounts of superparamagnetic iron oxide nanoparticles (SPIONs) were successfully synthesized by adding SPIONs into oil phase system via the emulsion method. All the obtained ECPSs possess open macropores in the shell and interconnected pores inside the spheres [38].

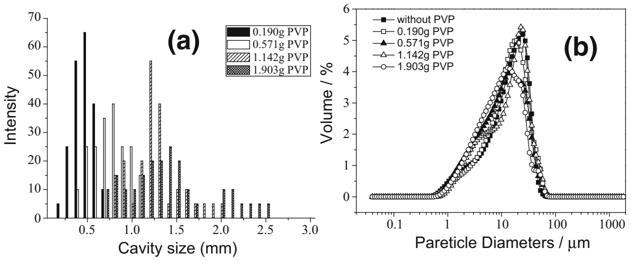

Fig. 31 Cavity size distribution (**a**) and size distribution (**b**) of the microspheres fabricated with different PVP contents [36]

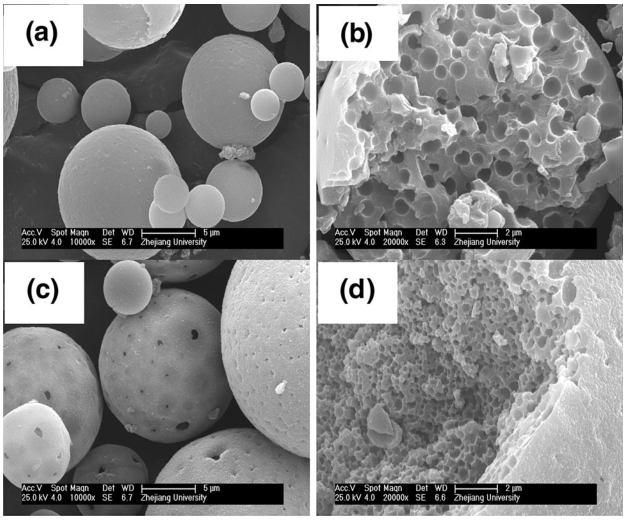

Fig. 32 SEM images of zirconia (**a**, **b**) and alumina microspheres (**c**, **d**) with incontinuous multicavities fabricated via the method presented [36]

4.5.1 *Control of morphology and internal structure of ECPSs–SPIONs*

The formation mechanism of the ethyl cellulose porous spheres (ECPSs) can be attributed to phase separation as depicted as above mentioned. As shown in Fig. 33, the

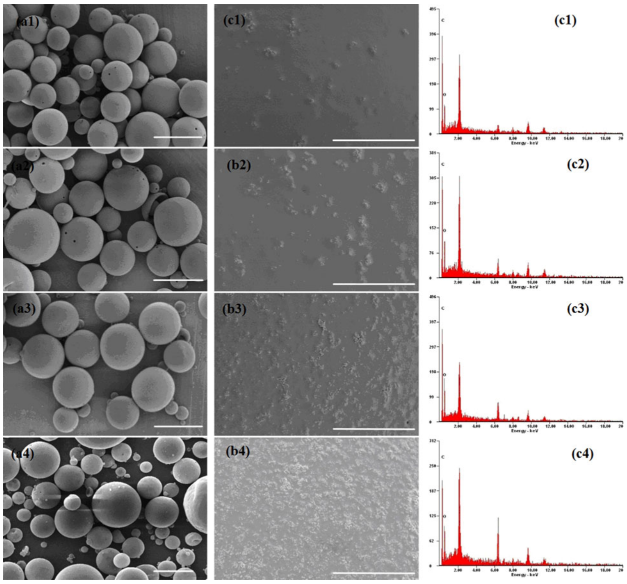

Fig. 33 SEM images and EDS analysis of ECPSs-SPIONs loaded with different amounts of SPIONs [38]

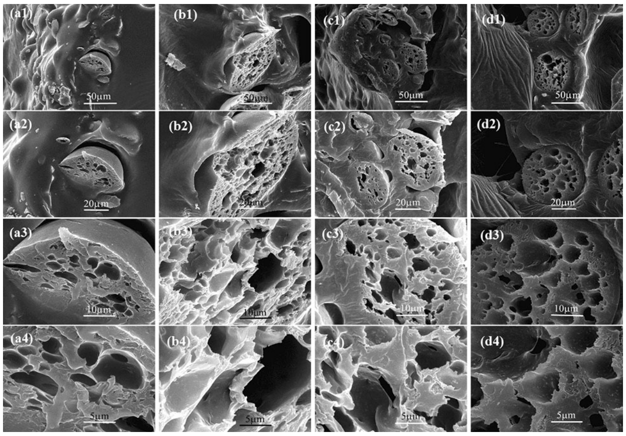

Fig. 34 Cross section of the ECPSs-SPIONs loaded with different loading amounts of SPIONs [38]

ECPSs–SPIONs are shown to be well spherical particles with a diameter size of around 40 μm and similar shape. All the obtained spheres possess open pores in their shells. The SPIONs uniformly distribute on the surface of the ECPSs, and the amount of SPIONs increases with the increase in SPIONs dispersion liquid.

From cross section of the ECPSs–SPIONs (Fig. 34), there exist cocontinuous porous structures in four samples, and the porous structures do not change with the increase in SPIONs dispersion liquid. The above results indicate that SPIONs are uniformly loaded on the ECPSs, and the loading.

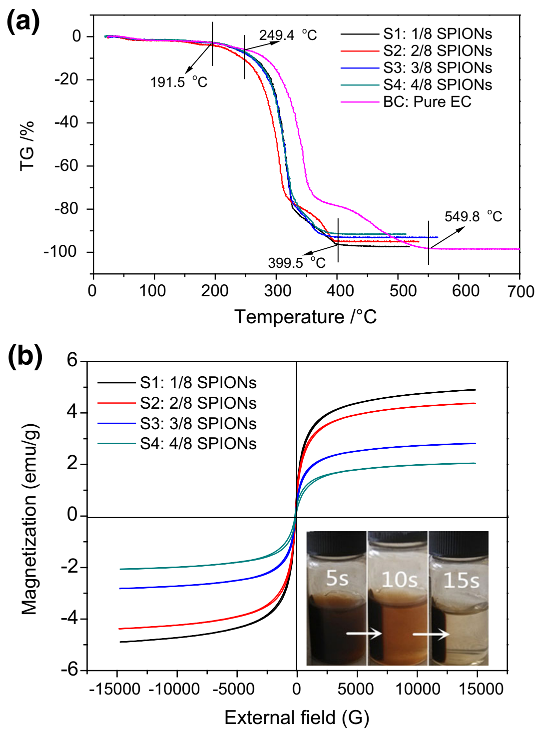

Fig. 35 Thermalgravity and magnetic hysteresis loop of ECPSs-SPIONs loaded with different loading amounts of SPIONs. (*Inset* pictures of ECPSs-SPIONs dispersed in water driven by an external magnet in 5, 10, and 15 s) [38]

4.5.2 *Application of ECPSs–SPIONs in magnetic-assisted separation*

As shown in Fig. 35, the loading of SPIONs has no effect on the morphology and porous structures of the ECPSs, while reduces the decomposition temperature of ECPSs. The addition of SPIONs increases the magnetization of the ECPSs–SPIONs and decreases the coercivity at room temperature. With the increase in the loading amounts of SPIONs, the saturation magnetizations of ECPSs–SPIONs increase and the coercivity decreases, respectively.

Due to their high magnetization, stable morphology, and other benign character of EC, the magnetized ECPSs are supposed to be applied in more areas, such as site-specific delivery and quick separation. More importantly, our work may have suggested a general method to synthesize ethyl cellulose porous spheres incorporated with useful nanoparticles.

5 The synthesis and application of metallic oxide aerogels by sol–gel process followed by surface modification and ambient pressure drying

5.1 Introduction

Aerogels are designated as dried gels with a very high relative pore volume, and are a class of mesoporous materials assembled by fine particles with network structure and gaseous dispersion mediums [3, 155, 156]. Aerogels are mesoporous solid materials composed of a three-dimensional network of nanoscale skeletons, and exhibit very high-surface-area and porosity, low-density, and a controllable structure. Aerogels are expected to be used as thermal and phonic insulators, electrodes, chromatographic packings, adsorbents, and catalyst supports [3].

As is well known, the drying process of gels is a key factor for the preparation of aerogels. During the conventional drying process of wet gels, a liquid–vapor meniscus is formed due to the surface tension of the liquid, and thus, a capillary pressure is built up in the pore walls of the gels, which is able to collapse most parts of the pore volume since most gels have weak network strength. To avoid this collapse, a CO_2 supercritical drying technique is usually applied during the preparation of low-density aerogel materials [157–160]. However, the CO_2 supercritical drying technique is a multistep and time-consuming production procedure and not a good choice for mass production. It is therefore desirable to develop new preparation methods for producing aerogels under conventional ambient pressure drying conditions. A number of approaches have been reported in the preparation of silica aerogels.

In this study, we demonstrated an improved sol–gel route followed by surface modification and atmospheric pressure drying to prepare metallic oxide aerogels such as SiO_2/TiO_2 [40], TiO_2 [41], and ZrO_2 aerogels [42].

5.2 Synthesis and application of porous SiO_2/TiO_2 composite aerogels

In recent years, the application of porous aerogel adsorbent in water pollution treatment has attracted much attention. The SiO_2/TiO_2 aerogel adsorbent has a multilevel pore structure with the great specific surface area and diffusion resistance. Besides the multilevel pore structure and great specific surface area, it is also important for the enhancement of the adsorption capacity of adsorbent to chemically modify the adsorbent. In this work, porous SiO_2/TiO_2 aerogels with high surface area are prepared via sol–gel process accompanied by phase separation using tetraethoxysilane and tetrabutyl orthotitanate as source of silica and titania, followed by ambient pressure drying to remove the solvents from the gels. The preparation proceeding shows that the morphology of porous structure and the size of the interconnected pores can be controlled by adjusting the compositions. The results show that SiO_2/TiO_2 aerogel is a kind of porous composite solid materials which is composed of dispersed nano-SiO_2 and TiO_2. The multilevel pore structures make composite powders have higher specific surface area and better adsorption performance. Structure change in the composite aerogels is the result of competition between phase separation process and sol–gel process essentially. Proper silicon content can refine the structure of SiO_2/TiO_2 composite aerogels dramatically. The prepared SiO_2/TiO_2 (3:1) aerogels not only exhibit bicontinuous channel structure (Fig. 36) and high BET surface area of 1000.5 m^2/g (Fig. 37), but also demonstrate multilevel pore structure. The adsorption process of Ce(IV) simulating Pu(IV) ions by the synthesized SiO_2/TiO_2 aerogels was studied.

The adsorption of Ce(IV) is carried out at same initial concentrations of 1400 mg L^{-1} at 35 °C. When the optimal adsorbent dosage is 6 g L^{-1}, the adsorption equilibrium time is 90, 105, 124 h, and the maximum adsorption capacities are 229.98, 212.52, 196.94 mg/g for SiO_2/TiO, SiO_2, and TiO_2 aerogels, respectively. By comparing the adsorption equilibrium time and the maximum adsorption

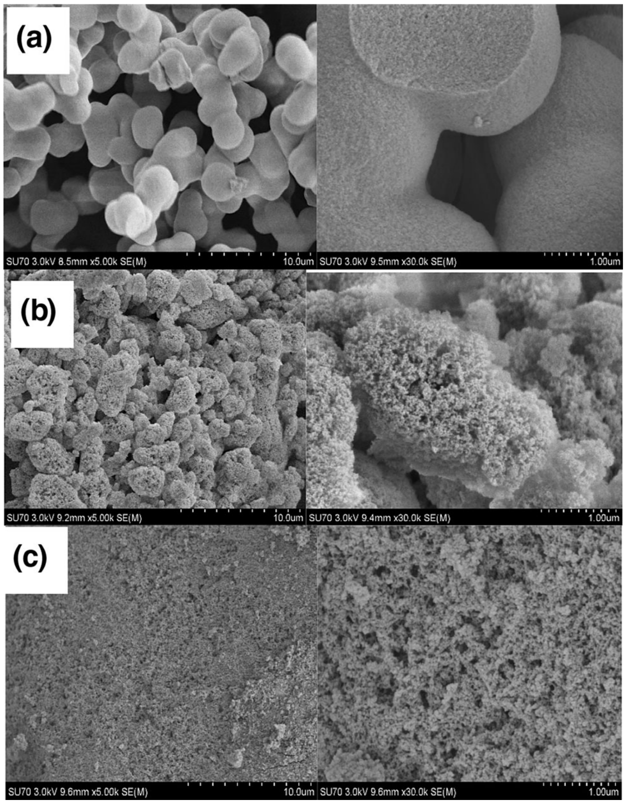

Fig. 36 SEM photograph: **a** SiO_2 powders; **b** TiO_2 powders; **c** SiO_2/TiO_2 composite aerogels with $n(Si)/n(Ti) = 3:1$ [40]

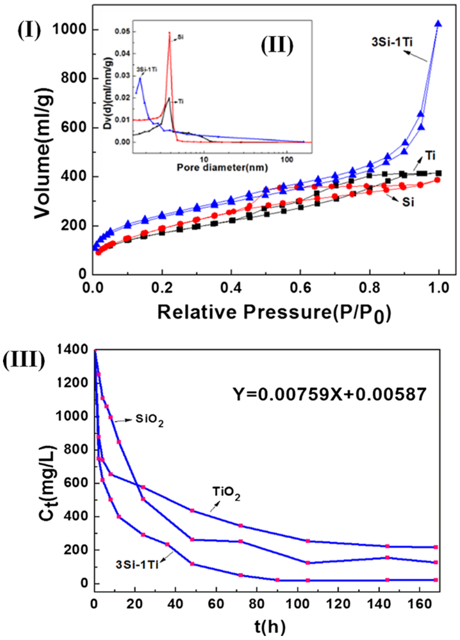

Fig. 37 N_2 adsorption–desorption isotherms (*I*), pore size distribution curves (*II*) and relationship between residual concentration and adsorptive time (*III*) of prepared aerogels: (a) SiO_2/TiO_2 aerogels with $n(Si)/n(Ti) = 3:1$; (b) SiO_2 powders; (c) TiO_2 aerogels [40]

capacities of the three aerogels, we can determine the contribution of high BET surface area (1000.5 $m^2\ g^{-1}$) and the multilevel pore structures of micropore (1–2 nm) and mesopore (2–20 nm) in SiO_2/TiO_2 aerogels to the efficiency and stability improvement. Pure SiO_2 particles have good dispersion performance toward TiO_2 particles. As a result, the SiO_2/TiO_2 aerogels exhibited a larger BET surface area than the SiO_2 aerogels (475.4 $m^2\ g^{-1}$) and TiO_2 aerogels (625.1 $m^2\ g^{-1}$). This indicates that the higher BET surface area can make the surface of the optimum SiO_2/TiO_2 aerogels has more adsorption sites to catch Ce(IV) ions and speed up the removal efficiency.

5.3 Preparation of monolithic titania aerogels by a sol–gel process combined with surface modification

Titania (TiO_2) aerogel is an important aerogel material combining catalytic activity, nontoxicity, good chemical stability of TiO_2 with low density, high surface area, and high porosity of aerogels [161–164]. The present monolithic or particulate TiO_2 aerogels are usually obtained by the supercritical drying. The process at such high pressures needs the use of expensive autoclaves, which restricts its industrial application due to production costs. In addition, TiO_2 aerogel has a weaker network skeleton than SiO_2 aerogel, and it is very difficult to prepare single TiO_2 aerogel (not composite aerogels, such as TiO_2–SiO_2 aerogel [40]) with monolithic shape and no cracking by ambient pressure drying. In the present work, monolithic titania (TiO_2) aerogels with high surface area were successfully synthesized by the sol–gel process combined with surface modification, followed by ambient pressure drying to remove the solvents from the gels. The effects of surface modification used polyethylene glycol (PEG) 2000 as surfactant on the gelation and microstructure of the aerogel were studied in detail [41].

5.3.1 *Effects of surfactant on the microstructure of aerogels*

After surface modification, the apparent density of TiO_2 aerogels slightly decreases and the corresponding porosity increases, with the increase in PEG 2000 content (Fig. 38). The apparent density and porosity of the TiO_2 aerogels without surface modification are 0.818 g cm^{-3} and 79 %, respectively, and the apparent density becomes the minimum as low as 0.716 g cm^{-3} and the corresponding porosity is about 81.6 %, when the molar ratio of PEG 2000:TBOT reaches to 0.005. With the further increase in PEO 2000 content, the apparent density increases and the corresponding porosity decreases.

From the morphology of fracture surface of TiO_2 aerogels with different PEG 2000 contents, compared with the aerogel without surfactant (Fig. 39g), the modified aerogel sample (Fig. 39e) shows a pore structure with smaller pore size and uniform pore size distribution. With the further increasing amount of surfactant, the macropore size becomes larger and the particles aggregate to form skeleton. The modified aerogel shows monolithic shape without cracks, although its outside is not smooth, as shown in Fig. 39h.

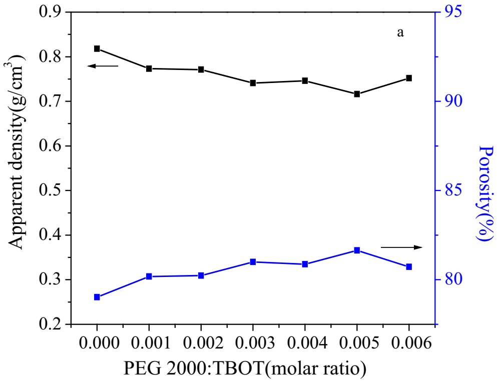

Fig. 38 Apparent densities and porosities of TiO_2 aerogels with different PEG 2000 contents [41]

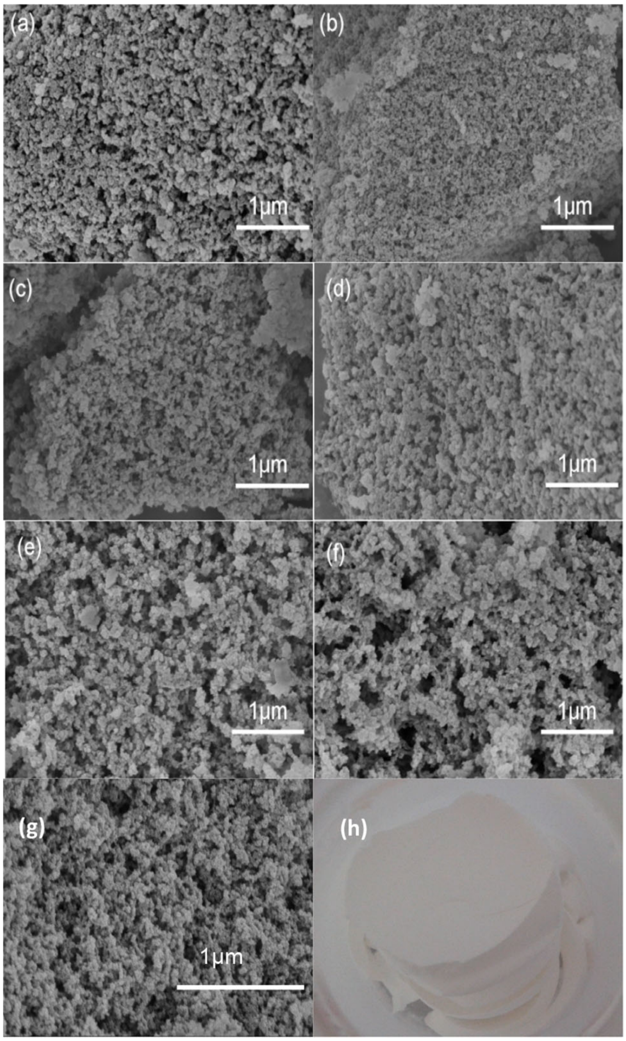

Fig. 39 Morphology of fracture surface of TiO_2 aerogels with different PEG 2000 contents. **a** PEG 2000:TBOT = 0.001, **b** PEG 2000:TBOT = 0.002; **c** PEG 2000:TBOT = 0.003; **d** PEG 2000:TBOT = 0.004; **e** PEG 2000:TBOT = 0.005; **f** PEG 2000:TBOT = 0.006; **g** without PEG; **h** monolithic aerogel with PEG 2000:TBOT = 0.005

5.3.2 *Effects of surfactant on the pore structure of aerogels*

The variation in the size and shape of the pores may be associated with the surface modification of PEG 2000. As shown in Fig. 40, the dried gel without surfactant possesses a surface area of 415 m^2 g^{-1} with a average pore size of about 8 nm and a whole pore volume of 0.86 cm^3 g^{-1}. The addition of surfactant (the sample with PEG 2000:TBOT = 0.005) increases surface area to 495 m^2 g^{-1} and increases the pore size to 10 nm and the pore volume to 1.181 cm^3 g^{-1}, respectively. With the further increases in surfactant (the sample with PEG 2000:TBOT = 0.006), the surface area decreases to 411 m^2/g, and the pore size and volume rapidly decrease to 8 nm and 0.84 cm^3 g^{-1}, respectively. As a result, the resultant aerogel with the PEG 2000:TBOB (molar ratio) of 0.005 exhibits specific surface area as high as 495 m^2 g^{-1}, apparent density of 0.716 g cm^{-3}, and porosity of 81.6 %.

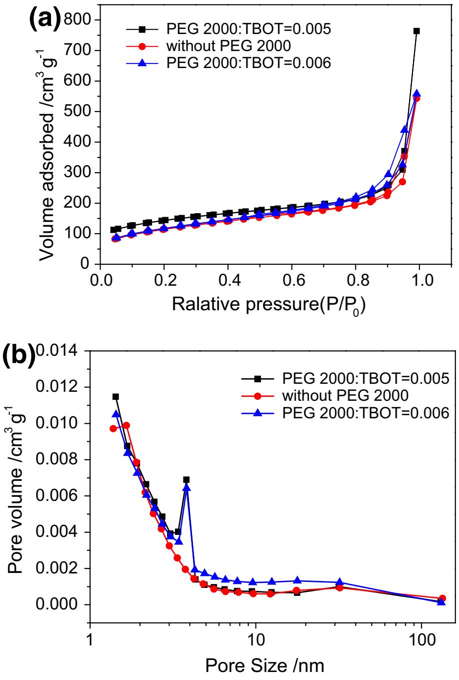

Fig. 40 N_2 adsorption–desorption isotherms and pore size distribution of the typical TiO_2 aerogels [41]

5.3.3 *Heat treatment of aerogel after surface modification*

Compared with the aerogels without heat treatment, the crystalline titania aerogel has a shrinkage about 10 %, while still keeps the shape and morphology before heat treatment (Fig. 41). The morphology is basically maintained after heat treatment. It indicates that the crystallization of aerogels after heat treatment does not spoil the monolithic shape and morphology of the aerogel basically. After heat treatment, the specific surface area decreases from 495 m^2 g^{-1} (before heat treatment) to 209 m^2 g^{-1}, which indicates that specific surface area still keeps a relative high value after heat treatment. The facile route provides a low-cost strategy for the preparation of metal oxide aerogels with high surface area. The monolithic TiO_2 aerogels will produce a lot of benefits and extend its application fields such as catalysis, separation, and absorption.

5.4 Synthesis of core–shell-structured zirconia aerogels by sol–gel process combining with atmospheric pressure drying

ZrO_2 aerogel has attracted much attention and has potential application in heat insulation materials because of their

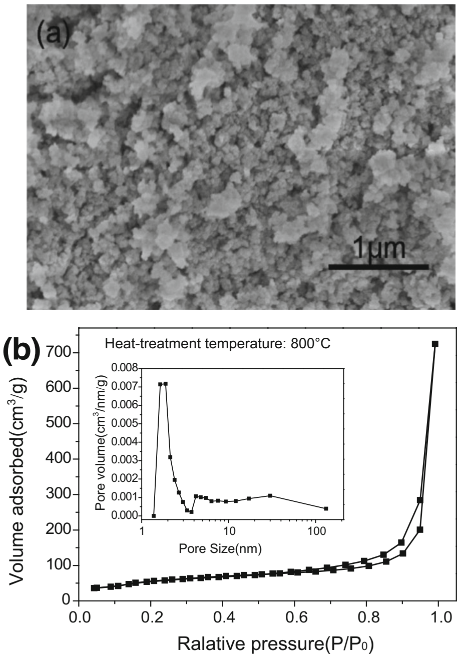

Fig. 41 Morphology (**a**) and N_2 adsorption–desorption isotherm (**b**) of aerogel heat-treated at 800 °C [41]

excellent properties combining zirconia with aerogel [165–168]. Many studies have been devoted to the synthesis of ZrO_2 aerogels by using supercritical drying. As is known, using supercritical drying enhances the network of ZrO_2 gel and prevents obvious shrinkage during drying; however, it is of high energy consumption and not a good choice for mass production. In this study, we demonstrate an improved sol–gel route followed by surface modification and atmospheric pressure drying to prepare ZrO_2 aerogel. In order to reduce the effect of capillary stress on gel skeletons during drying, formamide (FA), PEG 400, and tetraethoxysilane (TEOS) were used as drying control chemical additive, dispersant, and surface modifier, respectively. The effect of the amount of formamide and the concentration of tetraethoxysilane solution were investigated [42].

5.4.1 Overview of sol–gel process combining with atmospheric pressure drying

High-surface-area ZrO_2 aerogel can be obtained after atmospheric pressure drying mainly because of two factors (Fig. 42): (1) The utilization of FA as a gelation agent as well as a DCCA promotes the condensation process uniformly and modifies the polarity of gel skeletons; (2) the deposition of SiO_2 on the surface of primary particles forms a core–shell-like structure, which can resist the capillary stress better.

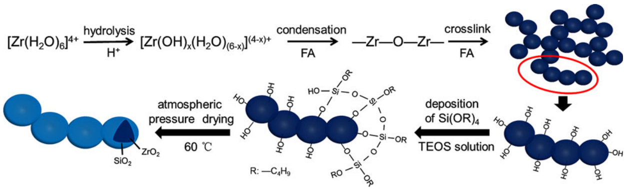

Fig. 42 Schematic representation of preparation of ZrO_2 aerogel in this study [42]

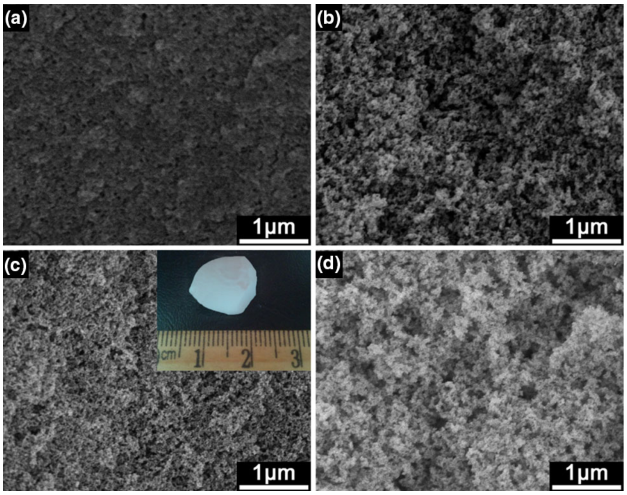

Fig. 43 SEM images of ZrO_2 aerogels prepared with varied amounts of FA: **a** molar ratio of Zr(IV):FA = 1:1.0, **b** Zr(IV):FA = 1:1.5, **c** Zr(IV):FA = 1:2.0, **d** Zr(IV):FA = 1:2.5. *Inset* shows the appearance of ZrO_2 aerogel [42]

5.4.2 Effect of drying control chemical additive

The SEM images (Fig. 43) of ZrO_2 aerogels prepared with varied amounts of FA show that when little FA is added, the gel exhibits obvious shrinkage after drying and few pores are observed (Fig. 43a). The morphology transforms to porous structure composed of loosely compacted particles with an increase in FA. Compared with the other samples, the pore size of the sample with Zr(IV):FA (mole) = 1:2.0 is homogeneously distributed and the as-dried gel exhibits a monolithic shape.

Nitrogen adsorption–desorption isotherms (Fig. 44) of ZrO_2 aerogels prepared with varied amounts of FA show that the BET surface area increases from 430 to 619 m^2/g, and the median pore size increases from 7.4 to 12.4 nm with the addition of FA; however, when too much FA is added, an obvious decrease in BET surface area is observed (520 m^2/g).

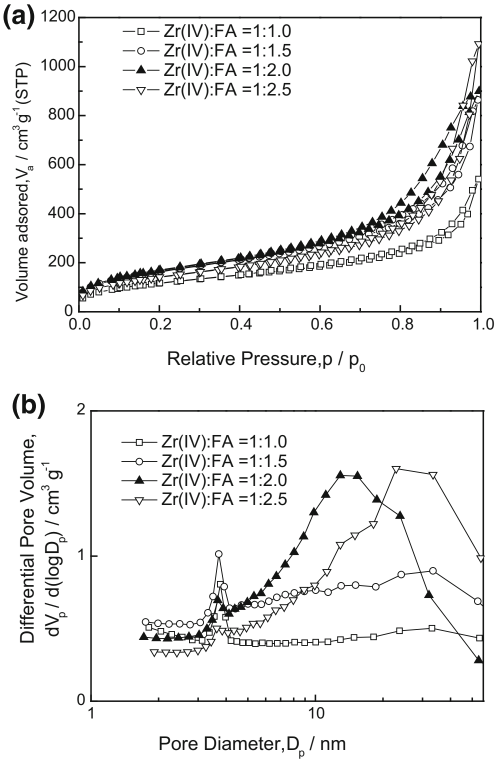

Fig. 44 **a** Nitrogen adsorption–desorption of ZrO_2 aerogels prepared with varied amounts of FA and **b** the corresponding BJH pore size distribution curve [42]

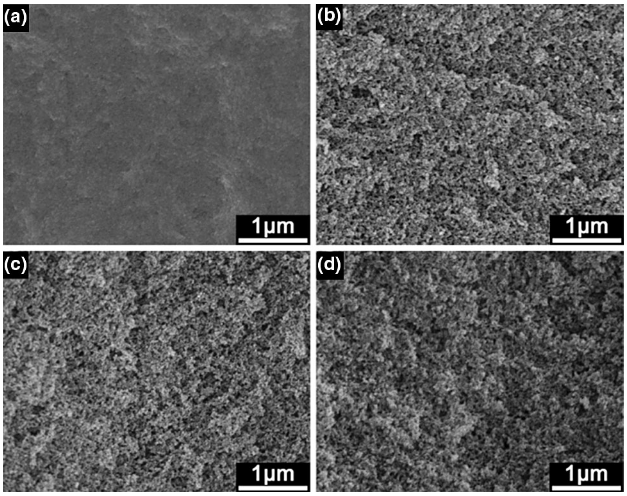

Fig. 45 SEM images of ZrO_2 aerogels immersed in TEOS solution with varied time: **a** 0, **b** 24 h, **c** 48 h, **d** 72 h [42]

5.4.3 *Effect of modification solution*

We investigated the effect of modification solution on the wet gels prepared from the starting compositions, as shown in Fig. 45. When dried in atmospheric pressure directly, the gel becomes fragments after drying, and almost no pores are observed even appropriate amount of FA is added (Fig. 45a). After immersed in TEOS solution for 24 h, aerogel with uniform mesoporous structure is obtained (Fig. 45b). And it seems that the morphology does not change much with a longer immersion time. For ZrO_2 aerogel immersed in TEOS solution for 48 h, the corresponding XP levels (Fig. 46) of O1s indicate that some SiO_2 generated from the hydrolysis of TEOS is deposited on the surface of ZrO_2 gel particles to form core–shell-structured aerogels.

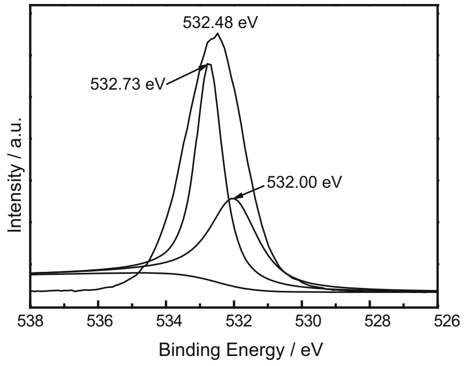

Fig. 46 O1s XPS spectra of ZrO_2 aerogel [42]

In summary, appropriate choice of formamide and tetraethoxysilane solution allowed the formation of core–shell-structured ZrO_2 aerogel with a BET surface area of 619 m^2/g and a pore size of 8.1 nm.

6 The fabrication and application of hierarchically porous monoliths by sol–gel process accompanied by phase separation

6.1 Introduction

Hierarchically structured porous materials, displaying multiple-level porosity integrated in a single architecture, have recently triggered extensive research because of their fascinating features such as high surface area, facilitated interface transport, and advanced mass transport kinetics [169–173]. Compared with single-sized porous materials, hierarchically porous materials in the form of monolith have more superior properties and applications [174–177]. The incorporation of mesopores into macroporous architectures offers an alternative strategy to greatly minimize diffusion barriers and potentially enhance the distribution of active sites. The reactants/products are able to enter/exit mesopores but experience attendant diffusion, such bimodal pore structures can significantly improve active site accessibility [178]. The comment synthesis strategy to prepare hierarchically structured porous materials is template method with various templates, such as dual and multiple surfactants, micelles, small solid particles, liquid drops, gas bubbles, and supramolecular aggregates. The present synthesis approaches have extended to combining the single surfactant-assisted procedure with supplementary chemical and/or physical methods such as aging, drying, phase separation, and post-treatment. Here, we report the preparation of three typical hierarchically porous monoliths (SiO_2, TiO_2, and ZrO_2) by sol–gel process accompanied by phase separation [43–47].

6.2 Spontaneous preparation of hierarchically porous silica monoliths with uniform spherical mesopores

Hierarchically porous silica monoliths with well-defined interconnected macropores and uniform spherical mesopores were spontaneously prepared by combining the polymerization-induced phase separation with epoxide-mediated sol–gel route without any complicated aging and drying and high-temperature heat treatment. Tetramethoxysilane (TMOS) and propylene oxide (PO) were used as the silica source and gelation mediation agent, and hydrochloric acid (0.01 mol L^{-1} HCl) and ethanol were the catalyst and solvent, respectively. The precise controlling for pore structures can be realized by using propylene oxide (PO) as the gelation mediation agent, poly(ethylene oxide)-block-poly(propylene oxide)-block-poly(ethylene oxide) (P123) as the phase separation inducer as well as the structure-directing agent and 1,3,5-trimethylbenzene (TMB) as the micelle-swelling agent [43].

6.2.1 Formation mechanism of hierarchically porous silica monoliths

As shown in Scheme 2, in the TMOS–HCl–PO–P123 system, the micelle-swelling agent TMB enters into the middle of P123 molecules and stabilizes the assemblage of P123-silica adducts in the whole process of sol–gel accompanied by phase separation, resulting in the expansion of mesopores and slight influence on macropores. After solvent exchange and drying process, TMB is removed.

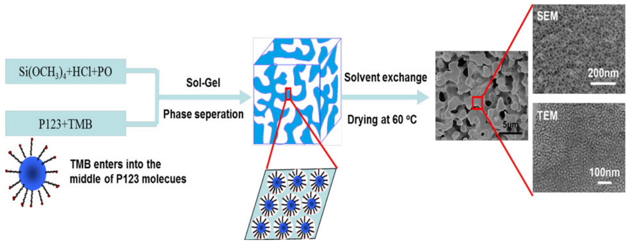

Scheme 2 Spontaneous preparation of pure silica monoliths having both well-defined interconnected macropores and uniform spherical mesopores [43]

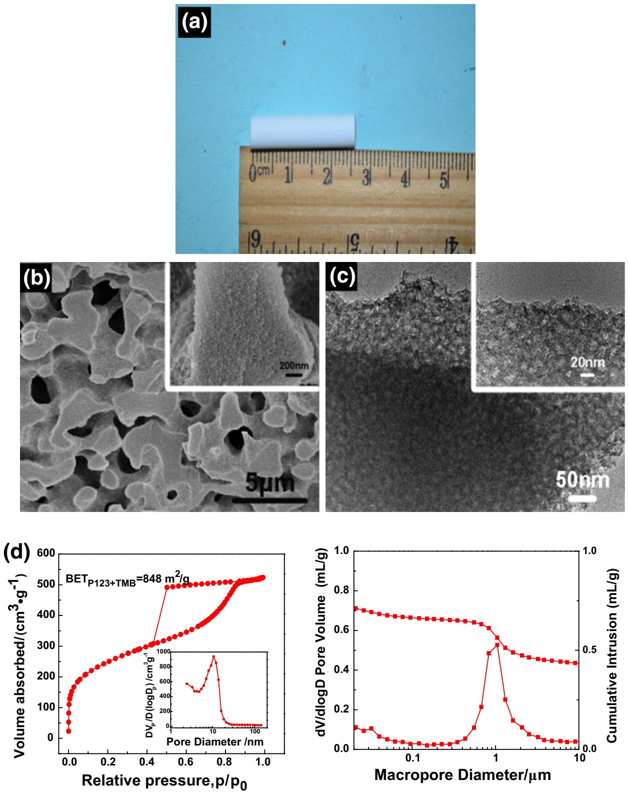

Fig. 47 Appearance (**a**), SEM (**b**) and TEM (**c**) images, and pore structure (**d**) of hierarchically porous silica monoliths [43]

6.2.2 Morphology and pore structures of hierarchically porous silica monoliths

From the appearance, SEM and TEM images, and pore structure of hierarchically porous silica monoliths (Fig. 47), the as-prepared silica dried gel exists in the form of monolith, possesses an interesting hierarchically porous structure constructed by 10 nm uniform spherical mesopores confined in macroporous framework of well-defined 1 μm macropores, and exhibits a BET surface area as high as 848 m^2 g^{-1}.

6.2.3 Thermal stabilization of hierarchically porous silica monoliths

Heat treatment at 400–1400 °C of the resultant hierarchically porous silica monolith (MPT4) was conducted to investigate the thermal stability of the macro-mesoporous structure as well as the influence of high temperature on the surface area of the monoliths as shown in Fig. 48. Heat treatment at 400–800 °C gradually decreases the BET

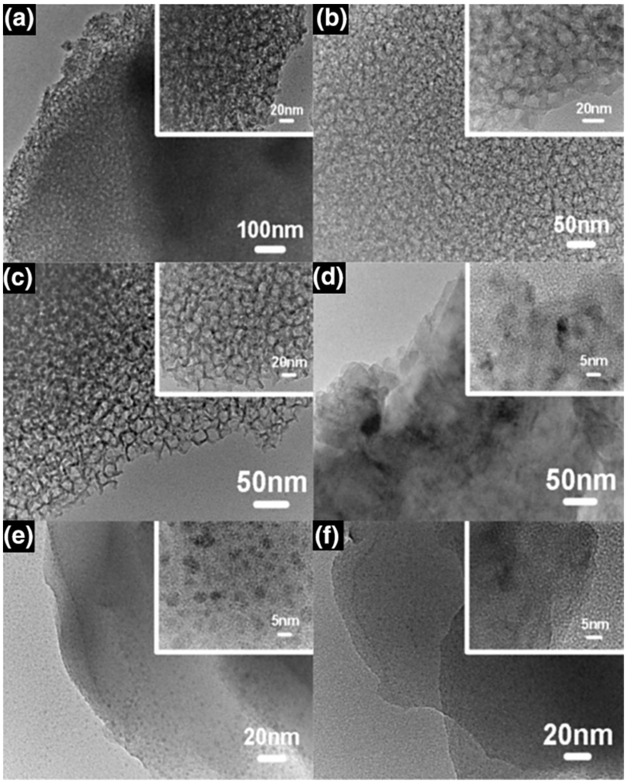

Fig. 48 TEM photographs of hierarchical porous silica monoliths (MPT4) at varied heat treatment temperatures: **a** 400 °C, **b** 600 °C, **c** 800 °C, **d** 1000 °C, **e** 1200 °C, **f** 1400 °C, and the *inset* pictures are HRTEM images [43]

surface area to 195 m^2 g^{-1}, while most of the uniform mesoporous structure remains intact. The resultant hierarchically porous silica monolith could be a promising material for a broad variety of application.

6.3 Sol–gel synthesis of nanocrystal-constructed hierarchically porous TiO_2-based composites

Titanium oxide (TiO_2) has received considerable attention because of its photoelectric properties, biocompatibility, and chemical stability and has been extensively applied in various kinds of fields such as photocatalysis [179, 180], sensing [181], dye-sensitized solar cells [182–184], and lithium-ion batteries (LIBs) [185–189]. In this work, hierarchically porous TiO_2-based composites (pure TiO_2 and TiO_2/Carbon (TiO_2/C) composite) were synthesized by a facile sol–gel process followed by post-calcination. Ionic precursor ($TiOSO_4 \cdot xH_2O$) was utilized as the titanium source, and the mixtures of distilled water and ethylene glycol were used as the solvents. Formamide was utilized to initiate gelation, and poly(vinylpyrrolidone) (PVP) acts as a phase separation inducer as well as a carbon source. The resultant TiO_2/C composite exhibits excellent cycling stability and superior rate capability as anode materials for LIBs [46].

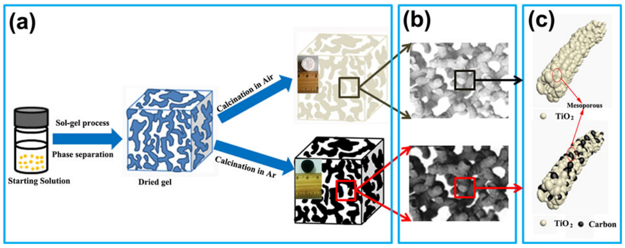

Fig. 49 **a** Schematic illustration of the experimental procedure of hierarchically porous TiO_2-based monoliths. **b** Macrochannels are derived from phase separation. **c** Mesoporous skeletons are composed of interconnected nanocrystals and in situ distributed carbon [44]

6.3.1 *Characteristics and functions of hierarchically porous TiO_2 monoliths*

As shown in Fig. 49, the as-prepared TiO_2-based composites reveal some distinguishing features: (1) Both of the pure TiO_2 and TiO_2/C composites show a hierarchically porous structure (Fig. 49b) with a high specific surface area, enlarging the contact surface between electrode and electrolyte. (2) The cocontiuous skeletons are constructed by many interconnected nanocrystals with sizes of 10–30 nm (Fig. 49c), which shorten the diffusion distance of Li-ion for the fast charge–discharge cycles. (3) During the procedure, PVP is used as a phase separation inducer as well as a carbon source resulting in the in situ formed TiO_2/C composites, which ensures an intimate contact of carbon and TiO_2, providing excellent electrical conductivity for high rate performance. The structure and electrochemical performance of pure TiO_2 and TiO_2/C composite calcined at different temperatures are investigated. The resultant TiO_2/C composite exhibits excellent rate and cycling performance due to the synergistic effect of the hierarchically porous structure resulting in large specific surface area and enhanced electrical conductivity ascribe to the in situ formed carbon derived from PVP.

6.3.2 *Morphology and pore structures of hierarchically porous TiO_2 monoliths*

Pure TiO_2 and TiO_2/C composite calcined at different temperatures demonstrates an interconnected macroporous structure (as shown in Fig. 50), and the typical size of cocontiuous macropores is in the range of 1–3 μm in diameter. The high-magnification SEM images (insets) reveal that the skeleton surface consists of many fine nanocrystals. With the increase in temperature, the porosity decreases due to the increase in average grain size, resulting in more compact skeletons.

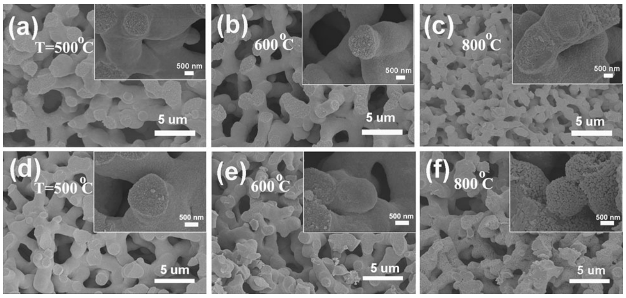

Fig. 50 SEM images of pure TiO_2 (**a**–**c**) and TiO_2/C composite (**d**–**f**) calcined at different temperatures. *Insets* are the corresponding high-magnification images [44]

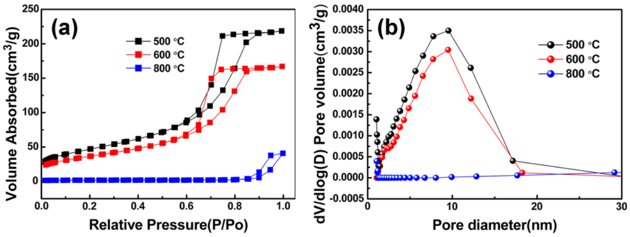

Fig. 51 Nitrogen adsorption–desorption isotherms (**a**) and pore size distributions curves (**b**) of TiO_2/C composite measured at 77 K [44]

Samples calcined at 500 and 600 °C present a typical type IV with H1 hysteresis loops at relative pressure of 0.65–0.85 according to IUPAC classification (Fig. 51), representing the mesoporous structure. The BET specific surface area of samples calcined at 500, 600, and 800 °C are identified to be 170, 132, and 7 $m^2\ g^{-1}$, respectively. The surface area and pore volume decrease as temperature increases, which could be ascribed to the effect of sintering and the growth of grains.

6.3.3 *Application of hierarchically porous TiO_2/C monoliths in lithium-ion batteries*

The hierarchically porous TiO_2/C composite shows excellent electrochemical performances with fast lithium-ion diffusion and electronic transport (Fig. 52), resulting from hierarchically porous structure and conductive carbon material. The TiO_2/C composite calcined at 500 °C exhibits superior cycling stability (delivers a remarkable discharge capacity of 132 mAh g^{-1} at 1 C after 100 cycles) and excellent rate capability (over 96 mAh g^{-1} at 30 C rate). We believe that this facile synthesis method can be extended to other composites (such as $Li_4Ti_5O_{12}$ and TiO_x) for a variety of energy conversion and storage applications.

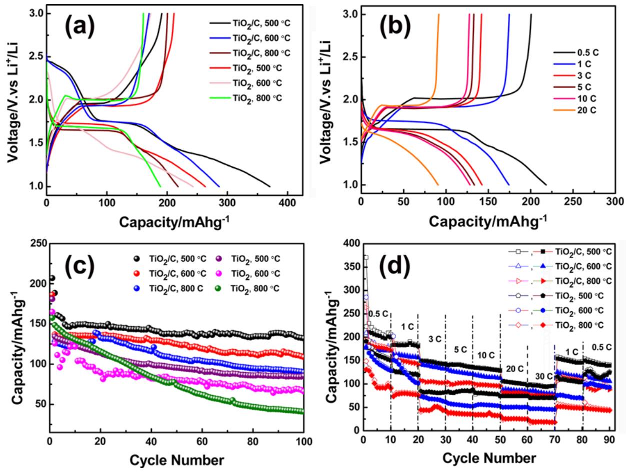

Fig. 52 Electrochemical properties of pure TiO_2 and TiO_2/C composite: **a** Initial charge and discharge curves at 0.5 C (1 C = 168 mAh g^{-1}). **b** Charge and discharge profiles (second cycle) of TiO_2/C composite calcined at 500 °C at different rates. **c** Cycling performance at 1 C. **d** Rate performance at various rates. All the tests are conducted with a voltage window of 1.0–3.0 V [44]

6.4 Preparation of hierarchically porous zirconia monoliths from ionic precursors with solvothermal treatment

As an important structural and functional material, zirconia (ZrO_2) has attracted considerable attention because of superior thermal, mechanical, chemical stability, electrical properties [190–192]. Zirconia has been extensively applied as an advanced material in various kinds of areas, such as electronic, optics, catalysis, and high-temperature structural engineering [193–199].

In this work, the novel and facile preparation of porous zirconia monolith via sol–gel process accompanied by phase separation was reported. The ionic precursors (zirconium oxychloride, $ZrOCl_2{\cdot}8H_2O$) are utilized to synthesize zirconia monolith in the presence of propylene oxide (PO) and poly(ethylene oxide) (PEO). The gelation of the system is mediated by PO, whereas PEO is added as a phase separation inducer. The resulting zirconia monoliths possess precisely controllable macropores at suitable starting compositions, and the solvothermal treatment of the resultant monoliths can further yield a tremendous number of mesopores on crystallized skeletons, leading to a remarkable increase in surface area [47].

6.4.1 *Morphology and pore structures of ZrO_2 monoliths*

Appropriate proportion of PO (0.52 mL) and PEO (0.105 g) can lead to concurrent sol–gel transition and

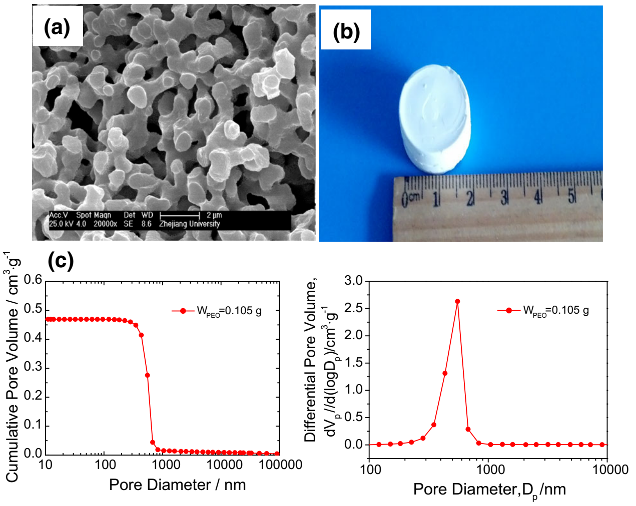

Fig. 53 SEM images (**a**), solid monolith (**b**), and pore structure (**c**) of macroporous ZrO_2 monoliths [47]

phase separation, producing cocontinuous porous structures. The system is divided into the cocontinuous gel phase and the fluid phase. The fluid phase is transformed into macropores after evaporation drying. As a result, monolithic dried gels with interconnected macropores and cocontinuous skeletons are obtained, as shown in Fig. 53. The macropore size of the dried gels is distributed roughly between 0.3 and 1 µm, and the median macropore size is 0.55 µm. The bulk densities of the three dried gels are 1.08 g cm^{-3} corresponding to 18.3 % of theoretical density (5.89 g cm^{-3}), the total pore volume is 0.473 cm^3 g^{-1}, and the total porosity is 51.2 %.

6.4.2 *Solvothermal treatment of macroporous ZrO_2 monoliths*

Solvothermal treatment of gels is introduced to study the effects on crystallization and modification of ZrO_2 skeletons. In this study, ethanol solution of ammonia was chosen as the solvent, and ZrO_2 monoliths were solvothermally treated with various ammonia concentrations at 180 °C for 12 h. Figure 54 shows the XRD patterns, SEM image, and pore structure of hierarchically porous zirconia monoliths with after solvothermal treatment with ammonia concentration of 2.0 mol L^{-1}. The peaks of tetragonal ZrO_2 crystallite become more and more sharp when the ammonia concentration increases from 0.5 to 2.0 mol L^{-1}. Solvothermal treatment with an ethanol solution of ammonia increases the number and size of the micropores and mesopores, thereby increasing the BET surface area from 171.9 to 583.8 m^2 g^{-1}. The presented synthesis process thus enables us to produce ZrO_2 monoliths having bimodal meso- and macroporous structures with adjustable pore sizes.

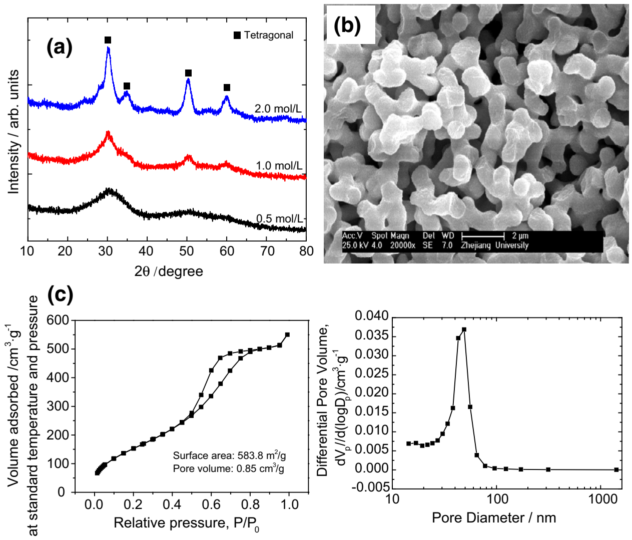

Fig. 54 XRD patterns (**a**), SEM image (**b**), and pore structure (**c**) of hierarchically porous zirconia monoliths with after solvothermal treatment with ammonia concentration of 2.0 mol L^{-1} [47]

7 Conclusions

Recent progress made in the synthesis of several sol–gel-derived materials was briefly reviewed. By combining with sol–gel process and other technologies, several typical materials (monodisperse nanoparticles, hybrid coatings, hollow microspheres, aerogels, and porous monoliths) possessing controllable shape, unique microstructure, superior properties, and special application were successfully synthesized for various areas of research and application fields. These aid technologies involve surface modification by using surfactants to inhabit nanoparticles interacting to agglomerate and obtain monodisperse nanoparticles, sol coating or dispersing particles to achieve in situ doping or uniform distribution of functional additives, organic–inorganic hybridization to enhance the microstructure uniformity and functional properties of coatings, templating induction followed by self-assembly to prepare mesoporous microcapsule loaded with functional nanoparticles, emulsion process accompanied by sol–gel reaction to fabricate hollow microspheres with incontinuous multicavities or interconnected pores, atmospheric pressure drying combining with surface modification to prepare metallic oxide aerogels, and cooperatively controlled phase separation parallel to sol–gel transition to fabricate hierarchically porous monoliths.

The above review and examples are not enough to demonstrate the abilities and advantages of sol–gel method combining with other technologies in the preparation of advanced materials. It is foreseeable that more and more new sol–gel-derived materials will be produced by sol–gel method, and a growing number of advanced technologies must be applied in the sol–gel process as significant aid.

Acknowledgments This work was supported by the National Natural Science Foundation of China (51372225), the Natural Science Foundation of Zhejiang Province, China (LY13B010001), and the High Science & Technique Brainstorm Project of Zhejiang Province of China (Grant No. 2014C01025).

References

1. Jeffrey Brinker C, Scherer GW (1990) Sol–gel science: the physics and chemistry of sol–gel processing. Academic Press, New York
2. Levy D, Zayat M (2015) The sol–gel handbook: synthesis, characterization and applications. Wiley-VCH, New York
3. Aegerter MA, Leventis N (2011) Aerogels handbook. Springer, New York
4. Guglielmi M, Kickelbick G, Martucci A (2011) Sol–gel nanocomposites. Springer, New York
5. Wright JD, Sommerdijk NAJM (2001) Sol–gel materials: chemistry and applications. CRC Press, Boca Raton
6. Dimitriev Y, Ivanova Y, Iordanova E (2008) J Univ Chem Technol Metall 43(2):181
7. Rahman IA, Padavettan V (2012) J Nanomater 2012:1
8. Grujić-Brojin M, Armaković S, Tomić N et al (2014) Mater Charact 88:30
9. Purcar V, Donescu D, Spataru IC et al (2013) Rev Roum Chim 58:37
10. Jung I, Gurav JL, Bangi UKH, Baek S, Park HH (2012) J Non-Cryst Solids 358:550
11. Iwamura T, Takasaki M (2015) Encycl Polym Nanomater 2015:1
12. Wu N (2010) J Ind Text 39:293
13. Nakanishi K (1997) J Porous Mater 4:67
14. Gaweł B, Gaweł K, Øye G (2010) Materials 3:2815
15. Kato M, Sakai-Kato K, Toyo'oka T (2005) J Sep Sci 28:1893
16. Hao YZ, Zhang QL, Zhang J, Xin CR, Yang H (2012) J Mater Chem 22:23885
17. Zhang QL, Wu F, Yang H, Zou D (2008) J Mater Chem 18:5339
18. Zhang QL, Wu F, Yang H (2011) Scrip Mater 65:842
19. Zhang QL, Yang H, Tong JX (2004) Rare Metal Mater Eng 33(Suppl. 3):133
20. Zhang QL, Yang H, Wang HP (2006) J Zhejiang Univ (Eng Sci) 40:1450
21. He Q, Yang H, Chen L et al (2014) Procedia Eng 94:37
22. He Q, Yang H, Chen L et al (2013) Adv Mater Res 815:80
23. He Q, Yang H, Chen L et al (2012) Electr Eng Mater 3:14 **(In Chinese)**
24. Guo XZ, Yang H, Zhu XY, Zhu L, Zhang LJ (2012) Mech Mater 46:11
25. Guo XZ, Yang H, Zhu XY, Zhang LJ (2013) Scrip Mater 68:281
26. Guo XZ, Zhu XY, Zhang LJ, Yang H, Fu PX, Gao LH (2010) J Chin Ceram Soc 38:258 **(In Chinese)**
27. Huang YP, Wu CC, Yang H, Que YS, Pan CG (2015) J Chin Ceram Soc 43:705 **(In Chinese)**
28. Wu CC, Yang H, Dong Z, Wu XR (2010) J Chin Ceram Soc 38:178 **(In Chinese)**
29. Lu JJ, Guo XZ, Yang H (2006) J Chem Ind Eng (China) 57:3511 **(In Chinese)**
30. Lu JJ, Guo XZ, Yang H (2005) Polym Mater Sci Eng (China) 22:211 **(In Chinese)**
31. Lu JJ, Guo XZ, Yang H, Zhang RJ, Zhang J (2006) Bull Chin Ceram Soc 25:133 **(In Chinese)**
32. Yang H, You WH, Shen QH et al (2014) RSC Adv 4:2793
33. Yang H, Liu Y, Shen QH, Chen LF, You WH, Wang XM, Sheng JS (2012) J Mater Chem 22:24132
34. Shen JC, Yang H, Shen QH, Feng Y (2013) J Mater Sci 48:7574
35. Shen JC, Yang H, Feng Y, Cai QF, Shen QH (2014) Solid State Sci 32:8
36. Cai WW, Yang H, Guo XZ (2014) Chin Chem Lett 25:441
37. Cai WW, Yang H, Guo XZ (2014) Procedia Eng 94:71
38. Yang H, Xie Y, Han DX, Mao WQ, Cai W, Guo XZ (2015) Colloid Polym Sci 293:1915
39. Yang H, Cai WW, Guo XZ, Zhang H (2013) Thermochim Acta 569:161
40. Fu YY, Ding XG, Meng M, Dou TJ, Yang H (2014) J Chin Ceram Soc 1:28
41. Yang H, Zhu WJ, Sun S, Guo XZ (2014) RSC Adv 4:32934
42. Ren J, Cai XB, Yang H, Guo XZ (2015) J Porous Mater 22:973
43. Guo XZ, Wang R, Yu H, Zhu Y, Nakanishi K, Kanomori K, Yang H (2015) Dalton Trans 44:13592
44. Guo XZ, Li WY, Zhu Y, Nakanishi K, Kanomori K, Yang H (2013) Acta Phys Chim Sin 29:646
45. Li WY, Guo XZ, Zhu Y, Yang H, Kanomori K, Nakanishi K (2013) J Sol Gel Sci Technol 67:639
46. Zhu WJ, Yang H, Nakanishi K, Kanomori K, Guo XZ (2015) RSC Adv 5:24803
47. Guo XZ, Song J, Lvlin YX, Nakanishi K, Kanomori K, Yang H (2015) Sci Technol Adv Mater 16:025003
48. Hyeon T (2003) Chem Commun 8:927
49. Dinh CT, Ngnyen TD, Kleitz F, Do TO (2009) ACS Nano 3:3737
50. Wang X, Zhuang J, Peng Q, Li YD (2005) Nature 437:121
51. Cozzoli PD, Pellegrino T, Manna L (2006) Chem Soc Rev 35:1196
52. Tseng CF, Huang CL, Yang WR (2007) Mater Lett 61:4054
53. Fu MS, Liu XQ, Chen XM (2008) J Eur Ceram Soc 28:585
54. Ferrarelli MC, Tan CC, Sinclair DC (2011) J Mater Chem 21:6292
55. Ogihara H, Randall CA, Trolier-McKinstry S (2009) J Am Ceram Soc 92:110
56. Nakazawa T, Naito A, Aruga T, Grismanovs V, Chimi Y, Iwase A, Jitsukawa S (2007) J Nucl Mater 367:1398
57. Hoshino T, Tanaka K, Makita J, Hashimoto T (2007) J Nucl Mater 367:1052
58. Ćosović V, Ćosović A, Talijan N et al (2012) Sci Sinter 44:245
59. Zheng J, Li SL, Song XZ et al (2012) Adv Mater Res 479:1986
60. Braunovic M, Konchits VV, Myshkin NK (2010) Electrical contacts fundamentals, applications and technology. CRC Press, Boca Raton
61. Pereñíguez R, Hueso JL, Gaillard F et al (2012) Catal Lett 142:408
62. Wathanyu K, Rojananan S (2012) Adv Mater Res 486:529
63. Asthana R, Ashok K, Narendra BD (2006) Nanomaterials and nanomanufacturing. In: Materials processing and manufacturing science. Elsevier, pp 551–614
64. Gadow R, Kern F, Killinger A (2008) Mater Sci Eng, B 148:58
65. Kireitseu M, Hui D, Tomlinson G (2008) Compos B 39:128
66. Guo ZH, Kin TY, Lei K, Pereira T (2008) Compos Sci Technol 68:164
67. Hyuncheol O, Sangsoo K (2007) J Aerosol Sci 38:1185
68. Karimian H, Babaluo AA (2007) J Eur Ceram Soc 27:19
69. Valter C, Cinzia DV (2004) Adv Colloid Interface Sci 108–109:167
70. Dafinone MI, Feng G, Brugarolas T, Tettey KE, Lee D (2011) ACS Nano 5:5078

71. Helsch G, Mös A, Deubener J (2010) Sol Energy Mater Sol Cells 94:2191
72. Wang XD, Shen J (2010) J Sol Gel Sci Technol 53:322
73. Shimizu W, Murakami Y (2010) Appl Mater Interfaces 2:3128
74. Chi FT, Yan LH, Lu HB, Jiang B (2011) Mater Lett 65:1095
75. Guillemot F, Brunet-Bruneau A, Bourgeat-Lami E (2010) Chem Mater 22:2822
76. Vicente GS, Bayón R, Germán N, Morales A (2011) Sol Energy 85:676
77. Osborne JH (2001) Prog Org Coat 41:280
78. Wang DH, Bierwagen GP (2009) Prog Org Coat 64:327
79. Zhludkevich ML, Salvado MI, Ferreira MGS (2005) J Mater Chem 15:5099
80. Moutarlier V, Neveu B, Gigandet MP (2008) Surf Coat Technol 202:2052
81. He XD, Shi XM (2009) Prog Org Coat 65:37
82. Chen Y, Wu CC (2010) Rare Met Mater Eng 39:288 **(in Chinese)**
83. Li CH, Jordens K, Wilkes GL (2000) Wear 242:152
84. Lee TH, Kang ES, Bae BS (2003) J Sol Gel Sci Technol 27:23
85. Li HY, Chen YF, Ruan CX et al (2001) J Nanopart Res 3:157
86. Wouters MEL, Wolfs DP, Van der Linde MC et al (2004) Prog Org Coat 51:312
87. Zhu ZF, He ZL, Li JQ, Zhou JQ, Wei N, Liu DG (2011) J Mater Sci 46:931
88. Jiang HY, Meng X, Dai HX, Deng JG, Liu YX et al (2012) J Hazard Mater 217–218:92
89. Zhang X, Zhang LZ, Xie TF, Wang DJ (2009) J Phys Chem C 113:7371
90. Tian LH, Ye LQ, Deng KJ, Zan L (2011) J Solid State Chem 184:1465
91. Xu F, Guo DF, Han HJ, Wang HX, Gao ZY et al (2012) Res Chem Intermed 38:1579
92. Zhang LS, Wang WZ, Chen ZG, Zhou L, Xu HL, Zhu W (2007) J Mater Chem 17:2526
93. Li JF, Lu GZ, Wang YQ, Guo Y, Guo YL (2012) J Colloid Interface Sci 377:191
94. He JY, Wang WM, Long F, Zou ZG, Fu ZY, Xu Z (2012) Mater Sci Eng, B 177:967
95. Xiang LQ, Zhao XP, Yin JB, Fan BL (2012) J Mater Sci 47:1436
96. Yang LX, Zhu YJ, Tong H, Liang ZH, Wang WW (2007) Cryst Growth Des 7:2716
97. Yuan CZ, Zhang XG, Su LH, Gao B, Shen LF (2009) J Mater Chem 19:5772
98. Hu J, Chen M, Fang XS, Wu LM (2011) Chem Soc Rev 40:5472
99. Chau NH, Bang LA, Buu NQ, Dung TTN, Ha HT, Quang DV (2008) Adv Nat Sci 9:241
100. Shi Q, Vitchuli N, Nowak J, Noar J, Caldwell JM, Breidt F, Bourham M et al (2011) J Mater Chem 21:10330
101. Senapati S, Srivastava SK, Singh SB, Mishra HN (2011) J Mater Chem 22:6899
102. Cui JH, Hu CF, Yang YH, Yang LF, Wang YL, Liu YL, Jiang ZY (2012) J Mater Chem 22:8121
103. Kim YH, Lee DK, Cha HG, Kim CW, Kang YS (2007) J Phys Chem C 111:3629
104. Ma JZ, Zhang JT, Xiong ZG, Yong Y, Zhao XS (2011) J Mater Chem 21:3350
105. Xiu ZL, Wu YZ, Hao XP, Zhang L (2011) Colloid Surf A Physicochem Eng Asp 386:135
106. Gu GX, Xu JX, Wu YF, Chen M, Wu LM (2011) J Colloid Interface Sci 359:327
107. Naro H, Shuster M, Awnir D (2011) J Sol Gel Technol 59:194
108. Xu WP, Zhang LC, Li JP, Lu YY, Li HH, Ma YN, Wang WD, Yu SH (2011) J Mater Chem 21:4593
109. Wang YG, Cao LN, Guan SW, Shi GN, Luo Q, Miao L et al (2012) J Mater Chem 22:2575
110. Roguska A, Pisarek M, Andrejcuk M, Lewandowska M, Kurzydlowski KJ et al (2012) Mater Res A 100A:1954
111. Liu X, Yu LM, Liu F, Sheng LM, An K, Chen HX, Zhao XL (2012) J Mater Sci 47:6086
112. Zhao YH, Zhou Y, Wu XM, Wang L, Xu L, Wei SC (2012) Appl Surf Sci 258:8867
113. Stevanovic MM, Skapin SD, Bracko I, Milenkovic M, Petovic J, Filipic M et al (2012) Polymer 53:2818
114. Kumar R, Howdle S, Münstedt H, Biomed J (2005) Mater Res Part B 75B:311
115. Kumar R, Howdle S, Münstedt H (2005) Biomaterials 26:2081
116. Rocks L, Faulds K, Graham D (2011) Chem Commun 47:4415
117. Uzayisenga V, Lin XD, Li LM, Anema JR, Yang ZL, Huang YF, Lin HX et al (2012) Langmuir 28:9140
118. Torres-Torres C, Tamayo-Rivera L, Rangel-Rojo R, Torrers-Martinez R et al (2011) Nanotechnology 22:355710
119. Ma ZJ, Ji HJ, Tan DZ, Dong GP, Teng Y, Zhou JJ, Guan MJ et al (2011) Nanotechnology 22:305307
120. Zhang ZT, Zhao B, Hu LM (1996) J Solid State Chem 121:105
121. Chou KS, Chen CC (2007) Microporous Mesopor Mater 98:208
122. Zhu ZF, He ZL, Li JQ, Zhou JQ, Wei N, Liu DG (2011) J Mater Sci 46:931
123. Jiang HY, Meng X, Dai HX, Deng JG, Liu YX, Zhang L, Zhao ZX, Zhang RZ (2012) J Hazard Mater 217–218:92
124. Zhang X, Zhang LZ, Xie TF, Wang DJ (2009) J Phys Chem C 113:7371
125. Tian LH, Ye LQ, Deng KJ, Zan L (2011) J Solid State Chem 184:1465
126. Zhang LW, Fu HB, Zhang C, Zhu YF (2006) J Solid State Chem 179:804
127. Zhou J, Song B, Zhao GL, Han GR (2012) Nanoscale Res Lett 7:217
128. Jiang DH, Hu WB, Wang HR, Shen B, Deng YD (2012) J Mater Sci 47:4972
129. Lu F, Cai WP, Zhang YG (2008) Adv Funct Mater 18:1047
130. Xu F, Guo DF, Han HJ, Wang HX, Gao ZY, Wu DP, Jiang K (2012) Res Chem Intermed 38:1579
131. Zhang LS, Wang WZ, Chen ZG, Zhou L, Xu HL, Zhu W (2007) J Mater Chem 17:2526
132. Li JF, Lu GZ, Wang YQ, Guo Y, Guo YL (2012) J Colloid Interface Sci 377:191
133. He JY, Wang WM, Long F, Zou ZG, Fu ZY, Xu Z (2012) Mater Sci Eng, B 177:967
134. Xiang LQ, Zhao XP, Yin JB, Fan BL (2012) J Mater Sci 47:1436
135. Kukushkin SA, Osipov AV (1998) J Exp Theor Phys 86:1201
136. Oskam G, Hu ZS, Penn RL, Pesika N, Searson PC (2002) Phys Rev E 66:011403
137. Hu ZS, Oskam G, Penn RL, Pesika N, Searson PC (2003) J Phys Chem B 107:3124
138. Yang LX, Zhu YJ, Tong H, Liang ZH, Wang WW (2007) Cryst Growth Des 7:2716
139. Yuan CZ, Zhang XG, Su LH, Gao B, Shen LF (2009) J Mater Chem 19:5772
140. Wang GZ, Saeterli R, Rorvik PM, van Helvoort ATJ, Holmestad R, Grande T, Einarsrud MA (2007) Chem Mater 19:2213
141. Shen F, Que W, Liao Y, Yin X (2011) Ind Eng Chem Res 50:91317
142. Cheng DL, Gao HC, Hao LJ, Cao XD, Wang YJ (2013) Mater Lett 111:238
143. Hu J, Chen M, Fang XS, Wu LM (2011) Chem Soc Rev 40:5472
144. Wang JZ, Sugawara-Narutaki A, Fukao M, Yokoi T, Shimojima A, Okubo T (2011) ACS Appl Mater Interfaces 3:1538

145. Zhu YF, Shi JL, Shen WH, Dong XP, Feng JW, Ruan ML, Li YS (2005) Angew Chem Int Ed 44:5083
146. Lai CY, Trewyn BG, Jeftinija DM, Jeftinija K, Xu S, Jeftinija S, Victor S-Y, Lin VSY (2003) J Am Chem Soc 125:4451
147. Wang LY, Bao J, Wang L, Zhang F, Li YD (2006) Chem Eur J 12:6341
148. Steaurra Stepban (1996) NASA Conf Publ 3425:26
149. Kim WS, Lee WY, Hyeon T (2002) J Chem Soc 124:7
150. Rogers TL, Wallick D (2012) Drug Dev Ind Pharm 38:521
151. Fernandez-Urrusono R, Gines JM, Morillo E (2000) J Microencapsul 17:331
152. Sahoo SK, Mallick AA, Barik BB, Senapati PC (2007) Pharmazie 62:117
153. Akbuga J (1991) Int J Pharm 76:193–198
154. Zhao YJ, Xie ZY, Gu HC, Zhu C, Gu ZZ (2012) Chem Soc Rev 41:3297
155. Alain CP, Gérard MP (2002) Chem Rev 102:4243
156. Daniel C, Alfano D, Venditto V (2005) Adv Mater 17:1515
157. Kanamori K, Aizawa M, Nakanishi K, Hanada T (2008) J Sol Gel Sci Technol 48:172
158. Kanamori K, Aizawa M, Nakanishi K, Hanada T (2007) Adv Mater 19:1589
159. Kanamori K, Nakanishi K (2011) Chem Soc Rev 40:754
160. García-González CA, Camino-Rey MC, Alnaief M, Zetzla C, Smirnova I (2012) J Supercrit Fluids 66:297
161. Malinowska B, Walendziewski J, Robert D (2003) Int J Photoenergy 5:147
162. Kim WI, Suh DJ, Park TJ (2007) Top Catal 44:499
163. Štengl V, Bakardjieva S, Subrt J et al (2006) Microporous Mesoporous Mater 91:1
164. Zhang L, Liang Z, Yang K (2012) Anal Chim Acta 729:26
165. Signoretto M, Oliva L, Pinna F, Strukul G (2001) J Non-Cryst Solids 290:145
166. Cimino S, Pirone R, Lisi L (2002) Appl Catal B 35:243
167. Bahamonde A, Campuzano S, Yates M, Salerno P, Mendioroz S (2003) Appl Catal B 44:333
168. Yamahara K, Sholklapper TZ, Jacobson CP, Visco SJ, De Jonghe LC (2005) Solid State Ion 176:1359
169. Zhang XY, Liu DX, Xu DD, Asahina S, Cychosz KA, Agrawal KV, Wahedi YA, Bhan A, Hashimi SA et al (2012) Science 336:1684
170. Lopez-Orozco S, Inayat A, Schwab A, Thangaraj S, Schwieger W (2011) Adv Mater 23:2602
171. Davis ME (2002) Nature 417:813
172. Yang XY, Su BL, Sanchez C (2012) Hierarchically structured porous materials: from nanoscience to catalysis, separation, optics, energy, and life science. Wiley-VCH, New York
173. Stevens SM, Loiola AR, Cubillas P (2011) Solid State Sci 13:745
174. Yang XY, Leonard A, Lemaire A, Tian G, Su BL (2011) Chem Commun 47:2763
175. Chen X, Wang X, Fu X (2009) Energy Environ Sci 2:872
176. Cao JL, Shao GS, Ma TY, Wang Y, Ren TZ, Wu SH, Yuan ZY (2009) J Mater Sci 44:6717
177. Zeng TY, Zhou ZM, Zhu J, Cheng ZM, Yuan PQ, Yuan WK (2009) Catal Today 147:S41
178. Gheorghiu S, Coppens MO (2004) AIChE J 50:812
179. Roy N, Sohn Y, Pradhan D (2013) ACS Nano 7:2532
180. Liu ZY, Sun DDL, Guo P, Leckie JO (2007) Nano Lett 7:1081
181. Wang G, Wang Q, Lu W, Li JH (2006) J Phys Chem B 110:22029
182. Huang JH, Hung PY, Hu SF, Liu RS (2010) J Mater Chem 20:6505
183. Pan K, Dong YZ, Tian CG, Zhou W, Tian GH, Zhao BF, Fu HG (2009) Electrochim Acta 54:7350
184. Stefik M, Heiligtag FJ, Niederberger M, Gratzel M (2013) ACS Nano 7:8981
185. Deng D, Kim MG, Lee JY, Cho J (2009) Energ. Environ Sci 2:818
186. Wagemaker M, Kentgens APM, Mulder FM (2002) Nature 418:397
187. Huang H, Yu ZY, Zhu WJ, Gan YP, Xia Y, Tao XY, Zhang WK (2014) J Phys Chem Solids 75:619
188. Huang H, Fang JW, Xia Y, Tao XY, Gan YP, Du J, Zhu WJ, Zhang WK (2013) J Mater Chem A 1:2495
189. Bi ZH, Paranthaman MP, Menchhofer PA, Dehoff RR, Bridges CA, Chi MF, Guo BK, Sun XG, Dai S (2013) J Power Sources 222:461
190. Tanabe K (1985) J Mater Chem Phys 13:347
191. Mercera P, Vanommen J, Doesburg E, Burggaaf A, Ross J (1991) J Appl Catal 71:363
192. Wirth H, Hearn MA (1995) J Chromatogr 711:223
193. Ortiz-Landeros J, Contreras-García ME, Pfeiffer H (2009) J Porous Mater 16:473
194. Wu CH, Chen SY, Shen P (2013) J Solid State Chem 200:170
195. Jung W, Hertz JL, Tuller HL (2009) Acta Mater 57:1399
196. Gionco C, Paganini MC, Giamello E, Burgess R, DiValentin C, Pacchioni G (2014) J Phys Chem Lett 5:447
197. Larsen G, Lotero E, Petkovic LM, Shobe DS (1997) J Catal 169:67
198. Diaz-TorresL A, De la Rosa E, Salas P, Romero VH, Angeles-Chavez C (2008) J Solid State Chem 181:75
199. Fonseca FC, de Florio DZ, Muccillo R (2009) Solid State Ion 180:822